4-2015

Numerical Investigation of Tonal Noise on a Transitional Airfoil under Varying Conditions

Warren W. Hiner
Embry-Riddle Aeronautical University - Daytona Beach

NUMERICAL INVESTIGATION OF TONAL NOISE ON A TRANSITIONAL AIRFOIL UNDER VARYING CONDITIONS

A Thesis

Submitted to the Faculty

of

Embry-Riddle Aeronautical University

by

Warren Hiner

In Partial Fulfillment of the

Requirements for the Degree

of

Master of Science in Aerospace Engineering

May 2015

Embry-Riddle Aeronautical University

Daytona Beach, Florida

NUMERICAL INVESTIGATION OF TONAL NOISE ON A TRANSITIONAL AIRFOIL UNDER VARYING CONDITIONS

by

Warren Hiner

A Thesis prepared under the direction of the candidate's committee chairman, Dr. Reda Mankbadi, Department of Aerospace Engineering, and has been approved by the members of the thesis committee. It was submitted to the School of Graduate Studies and Research and was accepted in partial fulfillment of the requirements for the degree of Master of Science in Aerospace Engineering.

THESIS COMMITTEE

Chairman, Dr. Reda Mankbadi

Co-Chair, Dr. Vladamir Golubev

Member, Dr. Anastasios Lyrintzis

Department Chair, Dr. Anastasios Lyrintzis
or Graduate Program Coordinator, Dr.Yi Zhao — Date 5/7/15

Dean of College of Engineering, Dr. Maj Mirmirani — Date 5/11/15

Associate VP for Academics, Dr. Robert Oxley — Date 5/11/15

TABLE OF CONTENTS

LIST OF TABLES

LIST OF FIGURES

SYMBOLS

u	Tangential velocity
v	Normal velocity
w	Spanwise velocity
$\vec{V}$	Velocity vector
ρ	Density
T	Temperature
p	Pressure
Re	Reynolds number
v	Viscosity
l	Length scale
φ	Disturbance vector
ω	Nondimensional frequency
f	frequency
α	Complex streamwise wavenumber
$-\alpha_i$	Disturbance growth rate
A	Disturbance amplitude
A_0	Initial disturbance amplitude
C_f	Coefficient of friction
τ_w	Wall shear stress

ABBREVIATIONS

BL	Boundary Layer
DNS	Direct numerical simulation
ILES	Implicit large eddy simulation
K-H	Kelvin-Helmholtz
LASTRAC	Langley Stability and Transition Analysis Code
LDA	Laser Doppler anemometry
LE	Leading Edge
LST	Linear stability theory
TE	Trailing edge
T-S	Tollmien-Schlicting

ABSTRACT

Hiner, Warren W. MSAE, Embry-Riddle Aeronautical University, May 2015. Numerical Investigation of Tonal Noise on a Transitional Airfoil Under Varying Conditions.

The generation of discrete acoustic tones is a problem of interest in transitional airfoils. Such tones exist for moderate Re below 2,000,000 and for low to moderate angles of attack. The purpose of this study is to use linear stability theory to study the growth of instabilities on the pressure and suction surfaces of airfoils for varying Re between 144,000 and 468,000 and angles of attack between 0˚ and 12˚. High accuracy 2D simulations based on an Implicit Large Eddy Simulation (ILES) code are conducted for a NACA0012 airfoil for varied conditions, and linear stability analysis is performed to predict amplification rates of disturbances within the boundary layers. The acoustic spectra and surface root mean square (RMS) pressure obtained from the high accuracy simulations are analyzed in conjunction with the stability results in order to explain the process of tone generation.

Our results indicate that the growth of instability waves in the flow-separation region is a necessary condition for the generation of tones, but the selected tonal frequencies are governed not only by vortex shedding, but also through a feed-back loop that is determined, in addition to the flow instability, by the trailing-edge scattering and the receptivity mechanisms. The predicted tonal frequency coincides with that of the shedding frequency and is lower than that predicted by Linear Stability Theory (LST) for maximum amplifications.

The tones disappear at higher incidence angles because the separation region on the suction side decreases. This leads to weaker instability-wave amplification and its

dependency on frequency weakens, thus disrupting the feed-back loop mechanism. Additionally, flow unsteadiness at the trailing edge inhibits consistent trailing edge scattering of acoustic waves.

At lower Re and moderate angles of attack, the suction surface is the primary surface responsible for the tones because of its larger separation bubble and stronger instability waves. As the Re increase, the separation region on the suction side diminishes, while instability growth on the pressure surface becomes stronger. Thus, the role of the suction side relative to that of the pressure in tone formation decreases with increasing Re.

1. Introduction

1.1. Motivation

Airfoils operating in the transitional regime with Re between 50,000 and 2,000,000 were found to be associated with discrete tonal noise. (e.g. Clark, 1971). There are several technologically-important applications that operate in this Re range. Examples include wind turbines, small aircraft, UAVs, fans, and rotors. For general aviation, it is imperative that noise mitigation techniques are developed to reduce community noise-pollution. For UAV reconnaissance platforms, it is important to suppress the noise to maintain stealth during operation. Therefore, the subject of this work is to address the mechanisms by which this tonal noise is generated.

1.2. Airfoil Noise

Airfoil noise can be classified as either broadband or tonal. Broadband noise is characterized by relatively homogenous distribution of sound over a range of frequencies. For turbulent airfoils, Brooks et al. (1989) have suggested that eddies, associated with the turbulent boundary layer, when convected past an airfoil with a sharp trailing edge are scattered as acoustic waves. This results in a broadband noise. If the trailing edge is blunt, it results in a pattern of shedding of coherent vortices. The pressure fluctuations of these vortices interact with the trailing edge to produce a higher intensity narrow-band tone. If the angle of attack is large, flow separation occurs and the flow becomes highly unsteady. The scale of turbulence at the trailing edge increases as the angle of attack increases, resulting in increased broadband noise at the trailing edge from the shedding of these vortices into the wake. In deep stall at very high angles of attack, the flow over the

entire suction surface is separated and noise radiates from the entire chord. The majority of noise contribution is broadband, but can still exhibit strong low frequency peaks due to the shedding of strong coherent vortices into the wake similar to the behavior of a bluff body.

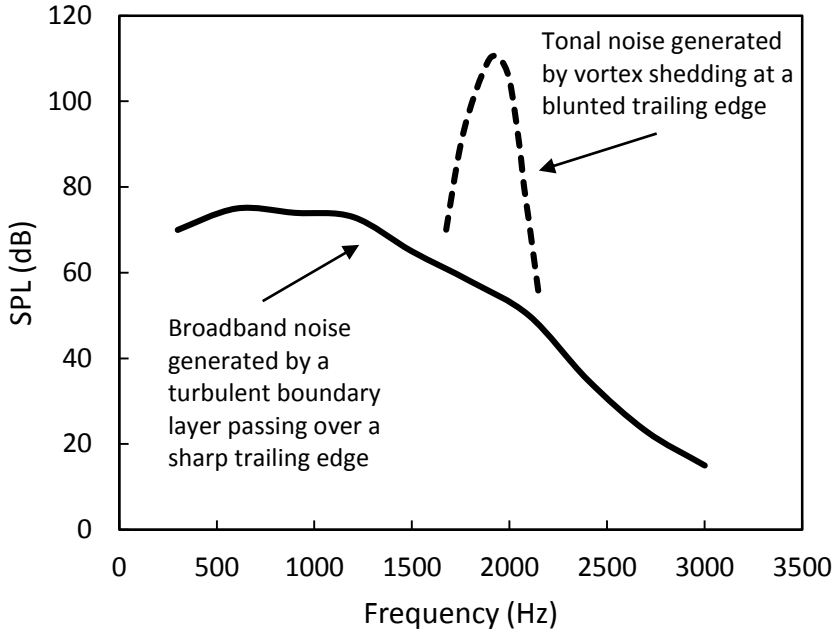

Figure 1.1. Example of tonal and broadband spectrums.

1.3. Characteristics of Transitional Airfoil Noise

The focus of the present study is on transitional-airfoil noise. It has been shown that if a laminar or transitional boundary layer exists on at least one side of an airfoil, discrete tones can be observed (Brooks et al. 1989). Boundary-layer instabilities moving along the airfoil roll up into vortices and are shed in the wake. Several authors, mentioned below, have suggested that there exists a feedback loop in which acoustic waves generated at the trailing edge or in the near wake region propagate upstream to

interact with the boundary layer disturbances, thus completing the loop.

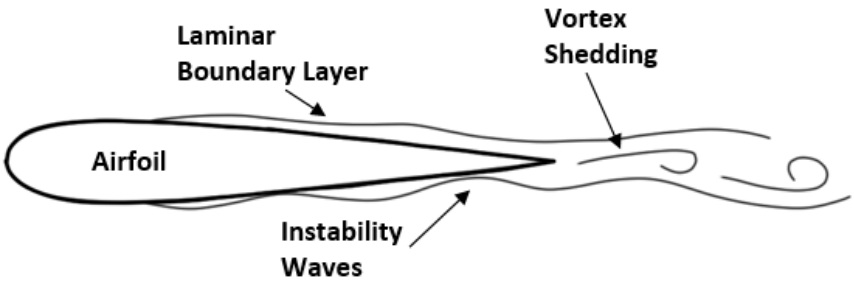

Figure 1.2. Noise from transitional vortex shedding (Brooks et al., 1989).

The tonal noise is characterized by several unique features:

1) *Multiple Tones:* When tonal noise is present for a transitional airfoil, it can be highly amplified above the background, as high as 40dB (Nash et al., 1999). It also possesses a unique spectrum that is characterized by multiple peak frequencies equidistantly spaced around a central peak frequency, shown in Figure 1.3.

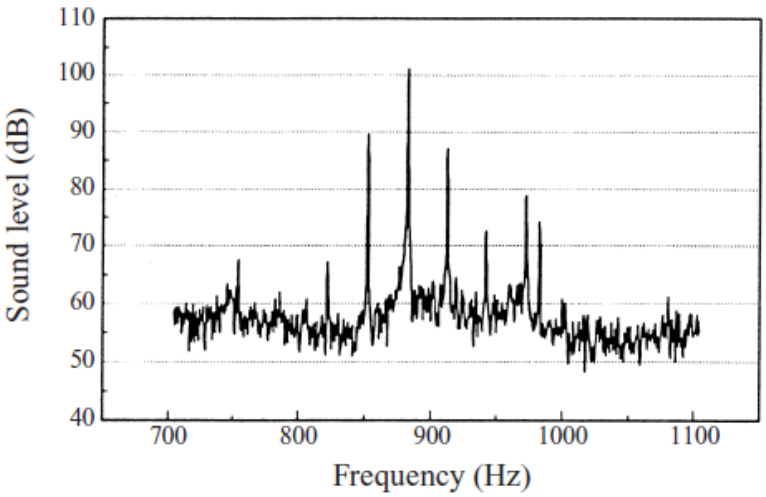

Figure 1.3. Tonal peaks in acoustic spectrum (Nash et al., 1999).

2) *Ladder-Structure:* Another unique characteristic of this noise mechanism is the existence of a ladder-type structure of frequency and velocity dependence. That is, as

the velocity increases for a given airfoil, the scattering frequencies increase as a function of $U^{0.8}$ on the "rungs" of the ladder. Plotting a line through the peak frequencies gives a relationship of $U^{1.5}$. These relationships can be seen in Figure 1.4.

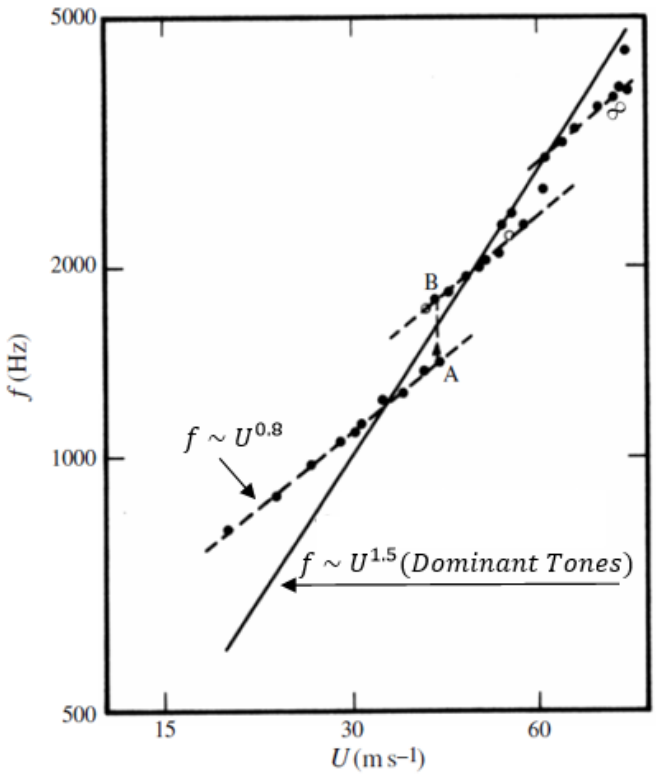

Figure 1.4. Ladder structure of tones (Petterson et al., 1973).

3) *Tonal Envelope:* Arcondoulis et al., 2010 have collected the past experimental data on transitional airfoil tonal noise. Their figure, shown here as Figure 1.5, indicates that there is a tonal envelope for the range of Re and angle of attack. For transitional airfoils, tones are only observed within this envelope.

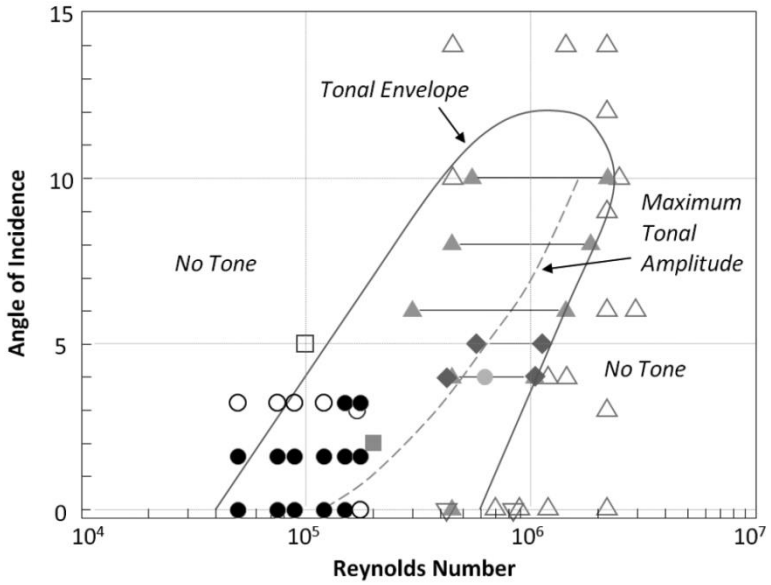

Filled markers represent that a tone was present, while unfilled markers represent that a tone was not present. Data sources: circles (Arcondloulis et al., 2009), triangles (Paterson et al., 1973), inverted triangles (Arbey and Bataille, 1983), squares, (Desquesnes et al., 2007), diamonds (Lowson et al., 1994), Tonal envelope and maximum amplitude line (Lowson et al., 1994).

Figure 1.5. Envelope of tonal noise (Arcondoulis et al., 2010).

1.4. Proposed Theories For Explaining Tonal Noise

There have been many proposed explanations for the generation of tonal noise on transitional airfoils with sharp trailing edges.

Patterson (1973), who had originally observed the ladder type structure, noted that the noise resembled the discrete-frequency vortex shedding associated with bluff bodies and proposed that a similar process was responsible for the observations of the airfoils. He formulated a scaling law based on a Strouhal number of 0.2, associated with bluff body shedding, referenced to twice the boundary layer thickness at the trailing edge. The result is the scaling law of $U^{1.5}$. However; Patterson offered no explanation for the multiplicity of tones or the discrete jumps in frequency and $U^{0.8}$ power relationship.

Tam (1974) disagreed with Patterson's explanation, pointing out that the vortex

shedding explanation was inadequate to explain the observations. Tam proposed that the ladder-type structure was due to an aerodynamic feedback loop. This is illustrated in Figure 1.6, in which disturbances originating at the sharp trailing edge travel downstream and induce lateral oscillations in the wake. Upon reaching a large enough magnitude, acoustic radiation is emitted and travels upstream, forcing the pressure side boundary layer to oscillate, thus completing the feedback loop. The alternative scaling law proposed by Tam references the length between the trailing edge and the acoustic source in the wake, whereas Patterson used the TE boundary layer thickness as the reference length.

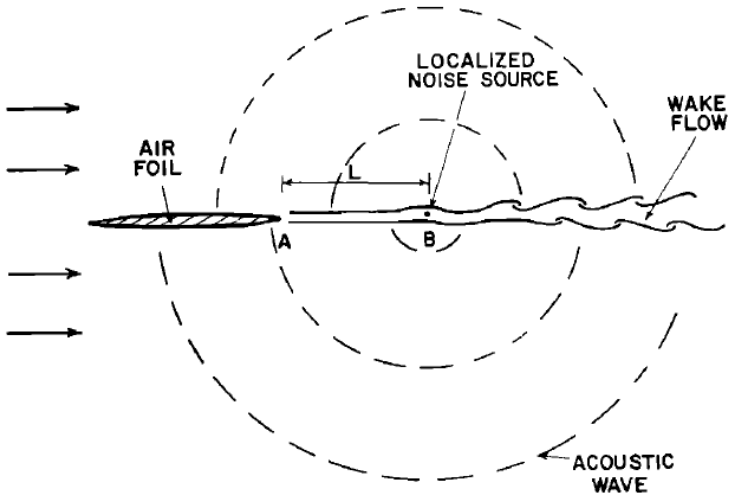

Figure 1.6. Feedback model proposed by Tam (1974).

Arbey and Bataille (1983) proposed another explanation by observing that there was significant similarity between broadband sound in the far-field with wall pressure spectrum near the trailing edge, which exhibited the same peak frequency. Their conclusion was that the broadband noise contribution was due to the growth of

instabilities in the boundary layer and their diffraction as acoustic waves at the trailing edge, similar to the generation of noise in a turbulent boundary layer. They also proposed that instability formation began at the maximum velocity point on the airfoil surface due to the beginning of the adverse pressure gradient in this region. In this model, shown in Figure 1.7, a mode becomes highly amplified if the acoustic waves from the trailing edge are in phase with the disturbances of the same frequency at the maximum velocity point. The scaling law formulated by Arbey and Bataille is a modified form of Tam's law with the reference length being the distance between the trailing edge and maximum velocity point on the airfoil.

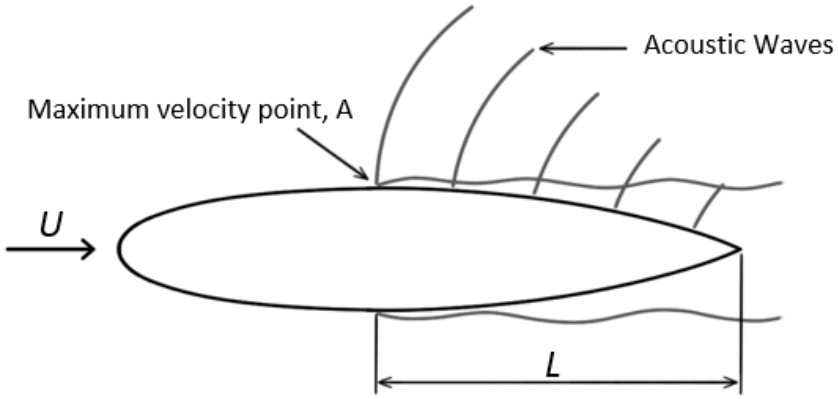

Figure 1.7. Feedback model proposed by Arbey & Bataille (1983).

Nash et al. (1999) using advanced laser-Doppler anemometry (LDA) techniques, found that the adverse pressure gradient on the pressure side leads to the development of inflectional boundary velocity profiles that develop into a region of separated flow near the trailing edge. As shown in Figure 1.8, an instability propagating downstream becomes massively amplified in this region and rolls up into a vortex. These vortices interact with the trailing edge to form a scattered oscillating field around the airfoil with

the same frequency as the most amplified instability. They proposed that this oscillating field provides the feedback mechanism to select the most amplified instability, and thus the observed discrete tone. Additionally, it was shown that the observed tone is very close to the most amplified disturbance frequency predicted by linear stability theory on the pressure side. These stability results will be discussed further in Section 2.5.

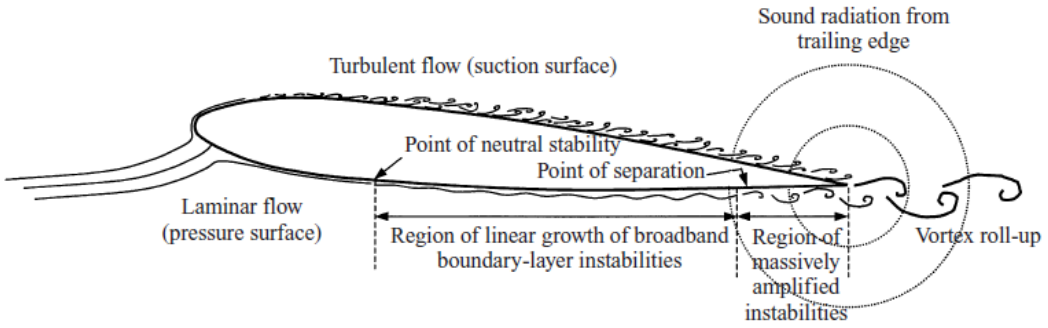

Figure 1.8. Feedback model proposed by Nash et al. (1999)

Desquesnes et al. (2007) extended Nash et al.'s (1999) work further by performing 2D direct numerical simulation (DNS) in order to explore the structure and role of flow on the suction surface, which had previously been neglected. They found that, as in the separation region shown on the pressure side by Nash et al., when tones are present there exists a point on the suction surface that is near separation which is conducive to the growth of instabilities. They showed by linear stability analysis that while the predicted most- amplified frequency on the pressure surface does correspond very closely with observed tone, there also exist highly amplified frequencies on the suction side as well a slightly different peak frequency. Therefore, it was proposed that an interaction between separate feedback loops on the upper and lower surfaces may have a role in the existence of multiple tones. The model proposed by Desquesnes et al.,

shown in Figure 1.9. It is very similar to that proposed by Nash et al. (1999), but includes a secondary loop that involves the amplification of Tollmien-Schlichting (T-S) waves on the suction surface of the airfoil.

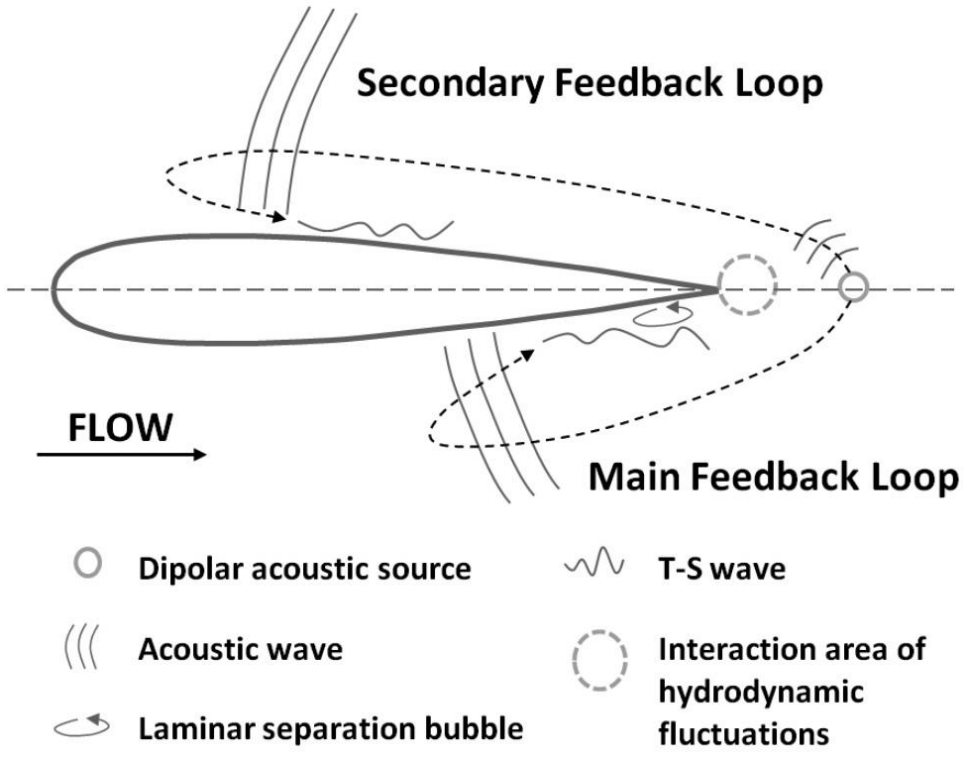

Figure 1.9. Feedback model proposed by Desquesnes et al. (2007).

1.5. Objective of Current Work

It had been previously shown (Paterson, 1973) that if the pressure side boundary layer was tripped, forcing it to become turbulent sufficiently early, the tonal noise could be eliminated. The work of Desquesnes et al. (2007) revealed that the pressure surface may have a hitherto unexplored role in the feedback mechanism that generates transitional airfoil tonal noise. However, recent experimental work performed by M.

Roger in Golubev et al. (2014) has shown that even if the pressure side or suction side is tripped, tones can still be observed. Figure 1.10 gives a contour map of Decibel levels for a range of velocities and frequencies. It can be seen that the tonal ladder structure is still observed when either the pressure side or the suction side is tripped. This leads to the speculation that at lower Re and moderate angles, sound generation and particularly the multiplicity of tones are related to processes on the suction surface, while interactions on the pressure surface seem dominant at higher Re.

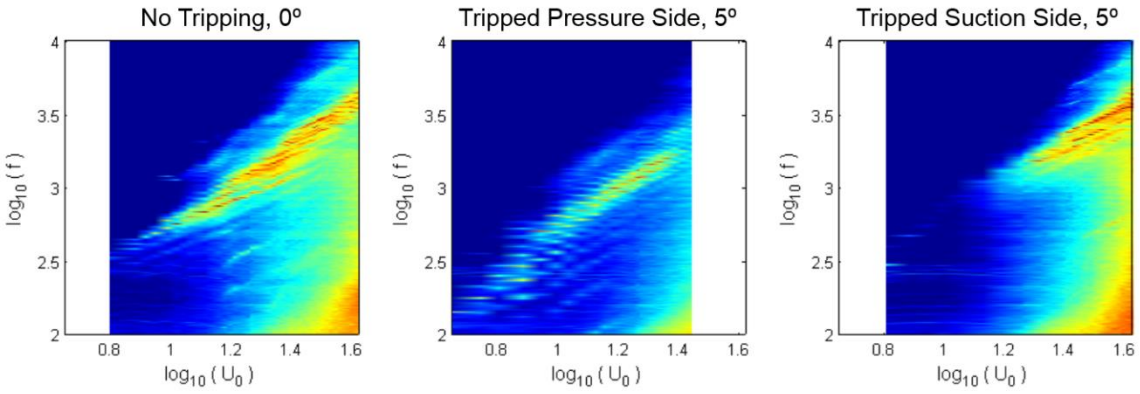

Figure 1.10. Effect of one-sided tripping (Golubev et al., 2014).

The goal of the present research, is therefore, to use linear stability analysis to further investigate the roles of the suction and pressures surfaces in the mechanism of tonal noise generation. To this end, a parametric study is carried out for several airfoils at Re between 144,000 and 468,000. This is done for angles of attack ranging from 0˚ to 12˚. The flow regime being investigated corresponds with the red lines in Figure 1.11. Thus, some of the conditions are within the expected range for tonal-noise generation and others are outside of it. Linear stability analysis is performed in order to predict the amplification of a range of frequencies on the pressure and suction surfaces of each

airfoil. These predictions are compared with the observed near and far-field acoustic spectrum, as well as other data gathered from ILES code results. The presence and effect of separation regions on both of the surfaces are of particular interest in order to understand the roles of the pressure and suction surfaces in the feedback mechanism.

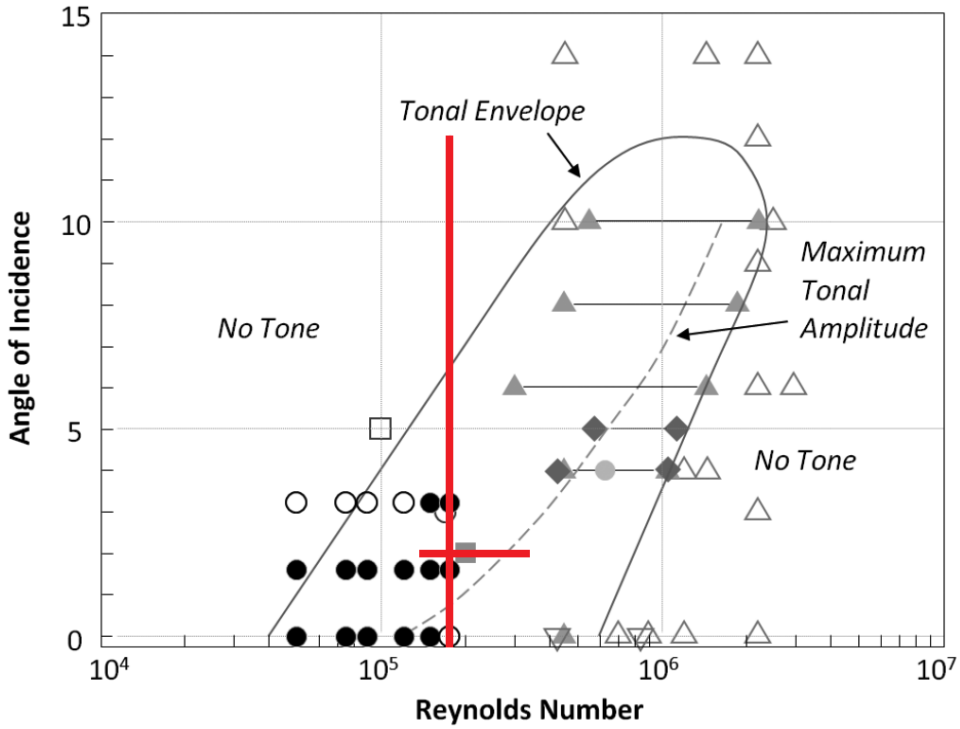

Filled markers represent that a tone was present, while unfilled markers represent that a tone was not present. Data sources: circles (Arcondloulis et al., 2009), triangles (Paterson et al., 1973), inverted triangles (Arbey and Bataille, 1983), squares, (Desquesnes et al., 2007), diamonds (Lowson et al., 1994), Tonal envelope and maximum amplitude line (Lowson et al., 1994). The red lines are the conditions examined in the present work.

Figure 1.11. Scope of current study.

2. Numerical Models

In this work we use three computational codes. The first one is an ILES code that provides the flow field. The flow field provides needed information such as the time-averaged flow, the RMS of the flow fluctuations, the location of flow separation, and the noise sources. The Ffowcs-Williams Hawkings (FWH) Code is then used to obtain the acoustic far-field based on the data provided by the ILES code. The linear stability code is then used (with the input from the ILES code) to see if it can explain the growth of the surface RMS pressure and the tonal noise. These codes are discussed below.

2.2. The ILES Code

We use a high-accuracy compressible viscous solver FDL3DI (Visbal and Gaitonde, 2002), which was developed at AFRL. The code employs a compact finite-difference scheme to discretize the spatial derivatives in the governing equations. For the present computation, the 6th order compact scheme (C6) is used (Lele, 1992). Higher-order methods are desirable in aeroacoustics, and the compact methods provide high-order accuracy using a small stencil. To calculate the values at point i the following formula is used:

$$\alpha\phi'_{i-1} + \phi'_i + \alpha\phi'_{i+1} = b\frac{\phi_{i+2} - \phi_{i-2}}{4} + a\frac{\phi_{i+1} - \phi_{i-1}}{2} \qquad (2.1)$$

Where α=0.376374, a = 1.5842493, b= 0.1684986. This scheme is implicit in space. For a 6th order method, a tri-diagonal system needs to be solved. Near the boundaries the order of the scheme is reduced to fourth-order compact (Gaitonde and Visbal, 1998). The time marching is accomplished by incorporating a second-order iterative, implicit approximately factored method described in (Visbal and Gaitonde, 2002). The compact

schemes, like other centered schemes, are susceptible to numerical instabilities. These numerical instabilities can arise from non-uniformity in the grid, the boundary conditions, and nonlinearity in the fluid flow. The code therefore uses a high-order implicit filtering technique. The filter is chosen to be at least two orders of accuracy higher than the difference scheme being utilized. The formula for the interior filtering is very similar to the equation for interior solutions,

$$\alpha_f \hat{\phi}_{i-1} + \hat{\phi}_i + \alpha_f \hat{\phi}_{i+1} = \sum_{n=0}^{F} \frac{a_n}{2} (\phi_{i+n} - \phi_{i-n}) \tag{2.2}$$

The $\hat{\phi}$ values are denoting filtered values while the ϕ is the unfiltered value. The order of accuracy of this filtering scheme is dependent upon the stencil size. α_f denotes the filtering coefficient, which is chosen to satisfy the inequality given by $-0.5 < \alpha_f < 0.5$ where a higher value of α_f corresponds with less filtering, and setting $\alpha_f = 0.5$ would imply no filtering. In these simulations was taken to be $\alpha_f = 0.4$. For an $8^{th,}$ order filtering a 9-point stencil is required. The F coefficients or a_0, a_1, a_N, are derived using Taylor- and Fourier-series analyses and these values are listed in Gaitonde and Visbal (1998), who also discusses the modifications to the filter near the boundaries**.**

Note that the governing equations are represented in the original unfiltered form, used unchanged in laminar, transitional, or fully turbulent regions of the flow. The resulting implicit procedure employs the high-order filter operator. The resulting filter thus selectively damps the poorly resolved, high-frequency content of the solution. This qualifies the codes as ILES.

In the numerical procedure, all variables are non-dimensionalized by the airfoil chord c and freestream flow density ρ_∞ and flow velocity u_∞. The employed numerical

approach was previously tested against various benchmarks and was successfully employed in flow control predictions, e.g., by Rizzetta et al (1999). The current version of the code employs the developed, and successfully tested, capability for the high-fidelity analysis of unsteady flow-structure interactions.

At high Re, the transition process becomes 3D. However, at low-to-moderate Re, for which the current results are conducted, computational results in Golubev et al. (2014) indicate that the differences between 2D & 3D are minimal for such Re.

2.3. The Acoustic Field Computation

Direct computation of acoustic data from the full Navier-Stokes equations requires a very fine mesh and accurate schemes in order to sufficiently resolve the acoustic fluctuations. This can be done relatively efficiently when modeling the sources of aerodynamic noise and the near-field region, but can become computationally expensive when attempting to predict sound characteristics at distances away from the source. Therefore, the problem must be divided into two calculations. The first is the CFD simulation of the source and near field, and the second is the prediction of the far-field sound via a surface integral method (Lyrintzis, 2003). One of the serface integral methods is the Ffowcs-Williams and Hawkings (FWH) method. This method is used herein to calculate the radiated sound based on the pressure near-field obtained by the ILES code. The FWH equation is an inhomogeneous wave equation derived by manipulating the continuity equation and the Navier-Stokes equations (Ffwocks-Williams & Hawkings, 1969). For a solid control surface, the surface integrals represent the contributions from monopole (thickness) ($p'_T(x,t)$ term shown below) and dipole

(loading) acoustic sources ($p'_L(x,t)$ term shown below), whereas the volume integrals represent quadruple (volume) sources in the region outside the control surface. For a permeable surface the first two terms lose their physical meaning, but the last volume integral term still denotes the quadruples outside the permeable surface. The method is based on solving the wave equation

$$\frac{1}{a_0^2}\frac{\partial^2 p'}{\partial t^2} - \nabla^2 p'$$

$$= \frac{\partial^2}{\partial x_i \partial x_j}\Big(T_{ij}H(f)\Big) - \frac{\partial}{\partial x_i}\{[P_{ij}n_i + \rho u_i(u_n - v_n)]\delta(f)\} \tag{2.3}$$

$$+ \frac{\partial}{\partial t}\{[\rho_0 v_n + \rho(u_n - v_n)]\delta(f)\}$$

$$T_{ij} = \rho u_i u_j + P_{ij}a_0^2(\rho - \rho_0)\delta_{ij} \tag{2.4}$$

$$P_{ij} = p\delta_{ij} - \mu\left[\frac{\partial u_i}{\partial x_j} + \frac{\partial u_j}{\partial x_i} - \frac{2}{3}\frac{\partial u_k}{\partial x_k}\delta_{ij}\right] \tag{2.5}$$

If we assume that the control surface contains all acoustic sources, the volume integrals outside this surface can be dropped, and the solution in the time domain becomes (for a stationary permeable surface):

$$p'(x,t) = p'_T(x,t) + p'_L(x,t) \tag{2.6}$$

$$4\pi p'_T(x,t) = \int_{f=0}\left[\frac{\rho_0(\dot{U}_n + U_{\dot{n}})}{r}\right]_{ret} dS + \int_{f=0}\left[\frac{\rho_0 U_n[r + a_0(M^2)]}{r^2}\right]_{ret} dS \tag{2.7}$$

$$4\pi p'_L(x,t) = \frac{1}{a_0}\int_{f=0}\left[\frac{\dot{L_r}}{r}\right]_{ret} dS + \int_{f=0}\left[\frac{L_r - L_M}{r}\right]_{ret} dS \tag{2.8}$$

$$+ \frac{1}{a_0}\int_{f=0}\left[\frac{L_r\{a_0(M_r - M^2\}}{r^2(1-M_r)^3}\right]_{ret} dS$$

$$U_i = v_i + \frac{\rho}{\rho_0}(u_i - v_i) \tag{2.9}$$

$$L_i = P_{ij}\hat{n}_j + \rho u_i(u_n - v_n) \tag{2.10}$$

The kernels of the integrals are computed at the corresponding retarded times,τ, defined as follows, given the receiver time, t and the distance to the receiver, r then

$$\tau = t - \frac{r}{a_0}$$

During the computation, the near filed variables computed by the ILES code are stored at the FWH surface every 44 steps. The pressure fluctuations at the observer's locations are then computed by the FWH surface integral acoustic method.

2.4. The Linear Stability Calculations

2.4.1. The Linear Stability Theory

Linear stability analysis is a tool that allows for the prediction of disturbance growth rates within a boundary layer or shear layer flow through a solution of the linearized Navier Stokes equations with certain applied assumptions. The disturbance vector ϕ is defined as

$$\phi = \left(p', u', v', w', T'\right)^T \tag{2.11}$$

Linear Stability Theory assumes that the mean flow evolves significantly more slowly in the streamwise direction than the wall-normal direction. Therefore, the flow at a given location is quasi-parallel. The disturbance mode shape, *X*, is assumed to have the form shown in (2.12) where ψ is an amplitude function. The disturbance vector is

assumed to have the form shown in (2.13) where ω is the frequency, β is the spanwise wave number and α is the streamwise wave number that is a function of beta and omega. For spatial analysis, ω and β are specified by the user, and α is the variable of interest in the numerical solution.

$$X(x,y) = \psi(y)e^{i\alpha x} \tag{2.12}$$

$$\phi(x,y,z,t) = \psi(y)e^{i(\alpha x+\beta z-\omega t)} \tag{2.13}$$

With

$$\omega = \frac{2\pi l}{u_e} f \tag{2.14}$$

$$\beta = \frac{2\pi}{\lambda_z} \tag{2.15}$$

$$\alpha = \alpha(\omega, \beta) \tag{2.16}$$

where ω is the temporal frequency and α is the streamwise wavenumber at a given location. Applying this assumption with a known set of mean flow profiles, the linearized Navier Stokes equations can be solved in order to obtain information about disturbances evolving within the flow. For this application, a spatial analysis is desirable in order to determine the disturbance growth rate at a given location on the airfoil surface. Therefore, α is variable of interest for a known set of frequencies. In this case, α is a complex number

$$\alpha = \alpha(\omega, \beta) = \alpha_r + i\alpha_i \tag{2.17}$$

where α_r is the real spatial wavenumber and $-\alpha_i$ is the instantaneous growth rate at a given streamwise location.

Knowing the growth rate at each location, it is possible by integration to obtain the total growth rate, *N*, for a disturbance at a given frequency.

$$N = \ln\left(\frac{A}{A_0}\right) = \int_{x_0}^{x} -\alpha_i \, dx \tag{2.18}$$

where A_0 is the initial disturbance amplitude, and A is the amplitude of the disturbance at a given streamwise location. The present study will primarily present the total amplification in this form, although some works discussed represent total amplification simply as A/A_0, which is equivalent to e^N. Figure 2.1 demonstrates the disturbance growth in terms of the neutral stability curve.

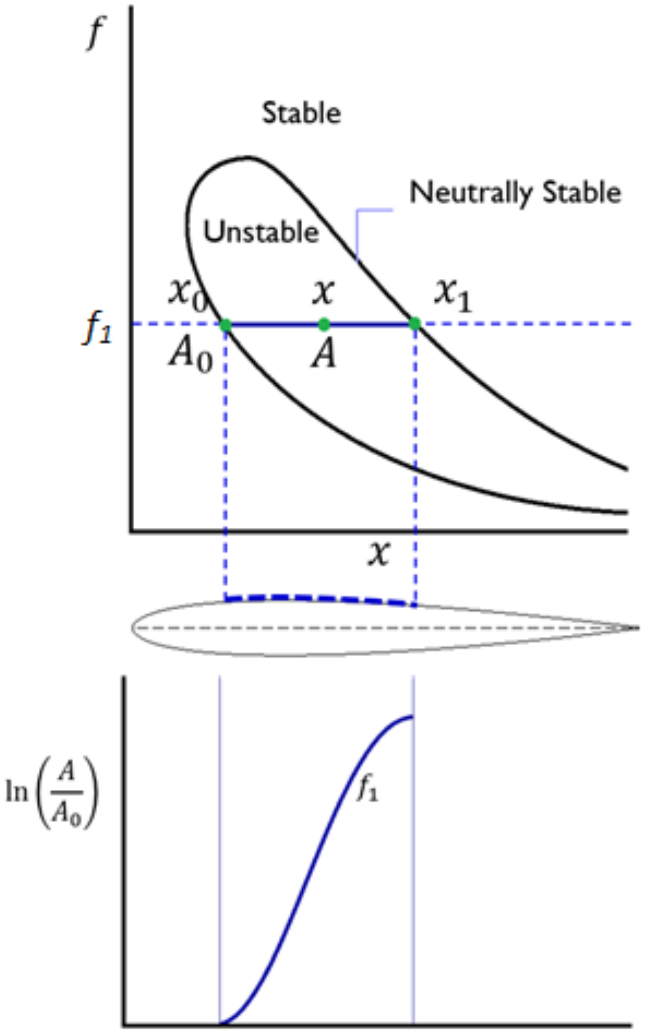

Figure 2.1. Explanation of instability growth.

The curve in the upper diagram of Figure 2.1 represents the line of neutral stability in the plane of chordwise location (x) and frequency (f). The region outside of this line is the stable region where all disturbances are damped and do not grow. The space inside of this line the unstable region where disturbances can become amplified. Consider a disturbance of arbitrary frequency f_1 moving downstream from the leading edge. This disturbance will remain damped until it reaches the first leg of the neutral stability curve at point x_0, where it has some initial amplitude A_0. Moving past this point, the disturbance enters the unstable region where it will continue to grow until crosses the second leg of the curve at point x_1, where it will once again become damped or saturated.

2.4.2. The Linear Stability Code, LASTRAC

We use here a linear stability code, LASTRAC developed by NASA Langley Research Center (Chang, 2004). The coordinate system employed by LASTRAC is a body-fitted system with x in the streamwise direction, y in the wall-normal direction, and z in the spanwise direction. The governing equations for this type of stability analysis are the linearized nondimensional Navier Stokes equations. The starting point is nondimensional non-linearized form of the Navier Stokes equations and the equation of state. To create the linearized form of the equations, the flow parameters are separated into two components: the mean laminar flow and the disturbance fluctuation, denoted by $\bar{q}$ and q' respectively.

$$q = \bar{q} + q' \tag{2.7}$$

The flow parameters, in their new form substituted into the non-dimensional

Navier Stokes Equations, and the mean flow equations are subtracted out so that only the governing equations for the disturbances remain. The new, linearized equations are shown in (2.8)

$$\Gamma\frac{\partial\phi}{\partial t}+\frac{A}{h_1}\frac{\partial\phi}{\partial x}+B\frac{\partial\phi}{\partial y}+\frac{C}{h_3}\frac{\partial\phi}{\partial z}+D\phi \quad = \\ \frac{1}{R_0}\left(\frac{V_{xx}}{h_1^2}\frac{\partial^2\phi}{\partial x^2}+\frac{V_{xy}}{h_1}\frac{\partial^2\phi}{\partial x\partial y}+V_{yy}\frac{\partial^2\phi}{\partial y^2}+\frac{V_{xz}}{h_3}\frac{\partial^2\phi}{\partial x\partial z}+\frac{V_{yz}}{h_3}\frac{\partial^2\phi}{\partial y\partial z}+\frac{V_{zz}}{h_3^2}\frac{\partial^2\phi}{\partial z^2}\right) \qquad (2.8)$$

In this equation, ϕ is the disturbance vector containing the fluctuations in pressure, velocity, and temperature, and the coefficient matrices Γ, A, B, C, D, and V_{ij} are the Jacobians of the flux vectors, similar to the typical CFD form of the Navier Stokes Equations.

$$\phi = \left(p', u',\ v',\ w',\ T'\right)^T \qquad (2.9)$$

By substituting the normal form of the disturbance discussed above into the linearized Navier Stokes Equations, applying the assumptions of linear stability theory, and neglecting viscous terms below the order of $1/R_0^2$, the governing equations take the form shown below.

$$\left(B+\frac{i\beta V_{yz}}{h_3R_0}-\frac{i\alpha V_{xy}}{h_1R_0}\right)\frac{d\psi}{dy} \\ +\left(D-i\omega\Gamma+\frac{i\alpha A}{h_1}+\frac{\alpha^2V_{xx}}{h_1^2R_0}-\frac{i\beta V_{xz}}{h_3R_0}+\frac{i\beta C}{h_3}+\frac{\beta^2V_{zz}}{h_3^2R_0}\right)\psi \qquad (2.15) \\ =\frac{V_{yy}}{R_0}\frac{d^2\psi}{dy^2}$$

$$\alpha = \alpha(\omega, \beta) = \alpha_r + i\alpha_i \tag{2.16}$$

The imaginary component is of the most interest because the sign of the amplification rate determines whether or not a mode is stable or unstable. It is unstable if $-\alpha_i$ is less than 0.

Boundary Conditions: The stability problem requires that boundary conditions be given at the ends of the domain in the wall-normal direction. At the wall, the no slip condition is used.

$$\hat{u} = \hat{v} = \hat{w} = \hat{T} = 0$$

The Dirichlet boundary condition is applied in the free stream.

$$\hat{u} = \hat{v} = \hat{w} = \hat{T} = 0, \qquad y \to \infty$$

Discretization and Solution: In LASTRAC, the equations are discretized via a first-order scheme in the streamwise direction and a fourth-order central difference scheme in the wall-normal direction. Near the boundaries however, the fourth-order scheme is replaced with a second-order scheme. The solution is then found as a two-step process. In the first step, viscous terms are neglected to recast the equation in a simpler linear form that can be solved an eigenvalue algorithms. The global eigenvalue spectrum obtained from these solvers will contain all discrete modes as well as the continuous spectrum. Unstable modes are identified, but they are not exact because of the viscous terms that were neglected.

Once the global eigenvalues are obtained, a local eigenvalue search is performed using the results from the global search as a starting point for using the iterative

Newton's method with the exact governing equations.

$$\alpha^{n+1} = \alpha^n - \tau^n / \left(\frac{\partial \tau}{\partial \alpha}\right)^n \tag{2.17}$$

In the local search, the goal is to get τ=0, which occurs when the iteration converges, yielding the exact values of alpha for the unstable modes.

2.5. How The Stability Results Will Be Used

We follow here the approach adopted by Nash et al. (1999) in using the stability results to interpret the observed flow and noise field results. This approach is outlined here:

- For each airfoil, boundary layer profiles were obtained for 12 chordwise locations on the pressure surface, shown in in Figure 2.2.
- The growth rates calculated from stability analysis for the tonal case, shown in Figure 2.3. In this example the highest growth rate happens at the trailing edge, and is at a frequency nearly identical to the observed tonal frequency.
- To obtain the N-Factor, the growth rates were integrated from station 1 to station 12 for each frequency to determine the total amplification at the trailing edge for each frequency. As can be seen from Figure 2.4, the observed tone, measured at 0.1 m behind the airfoil trailing edge, agrees very closely with the most amplified frequency predicted by stability analysis.
- The growth rate for this identified peak frequency (1048 in this example) is shown in Figure 2.5. The figure shows that the vast majority of growth takes place within the last few centimeters before the trailing edge, in the region where the flow has formed a separated shear layer.

If the amplification rates were found to be very weak, then this should lead to the suppression of tones, or that one or more components of the feedback-loop were missing and the amplification was not sufficient to initiate tonal noise generation.

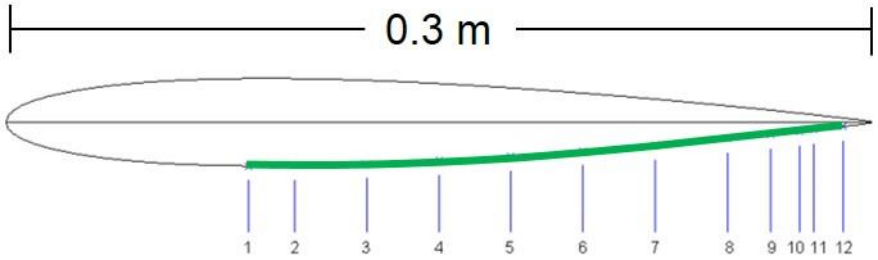

Figure 2.2. Boundary layer profile locations (Nash et al., 1999)

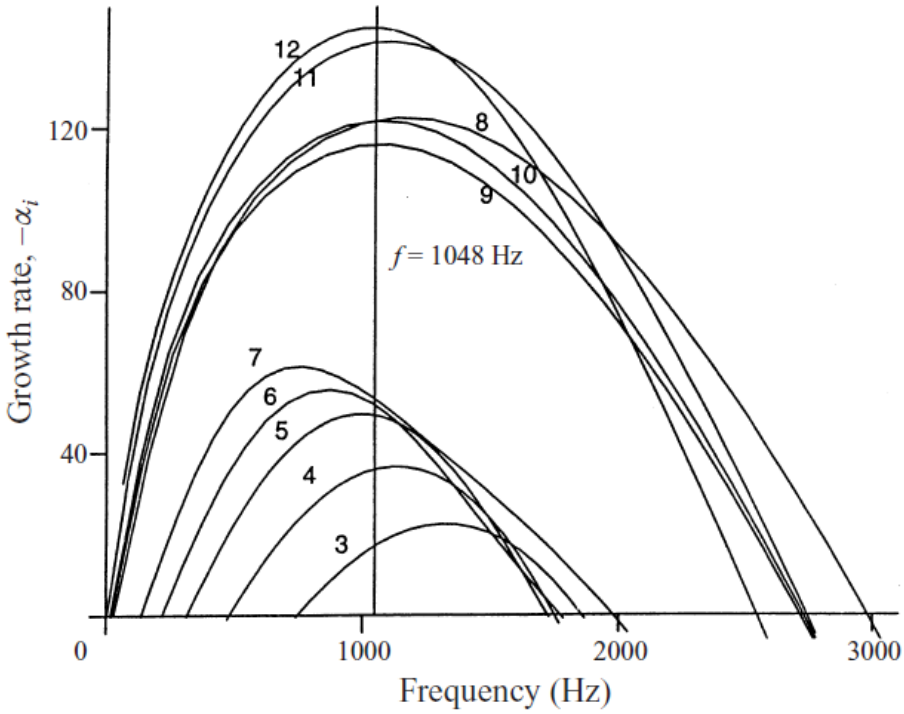

Figure 2.3. Growth rates at chordwise stations (Nash et al., 1999)

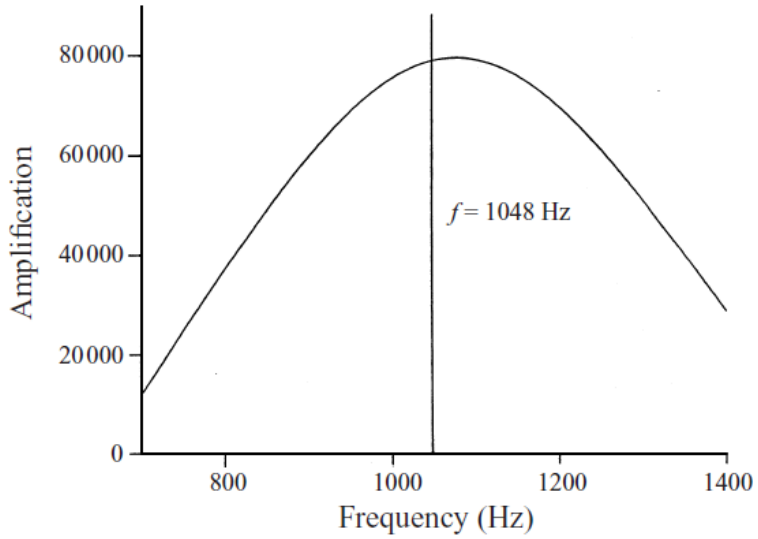

Figure 2.4. Instability amplification at station 12 for tonal cases (Nash et al., 1999).

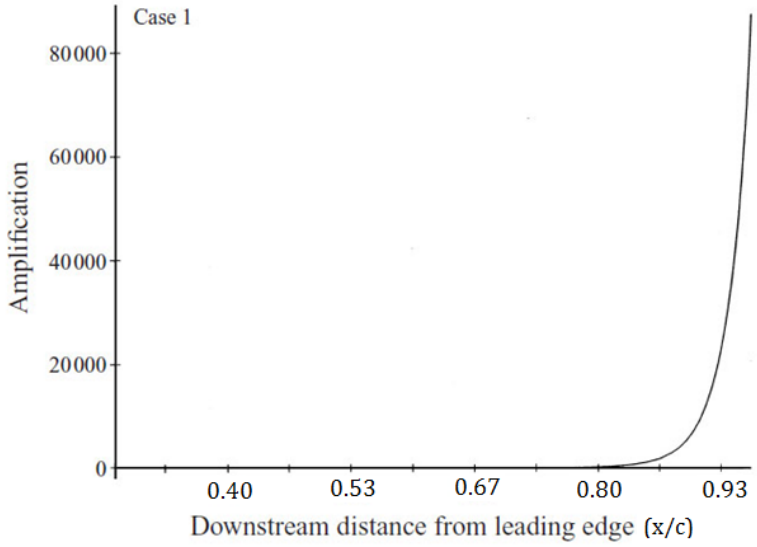

Figure 2.5. Chordwise amplification at 1048 Hz. (Nash et. al, 1999)

3. Results

Our objective here is to understand the generation of the acoustic tones at various incidence angles and Re and the role of the pressure and suction sides of the airfoil. For this purpose, we first fix the Re at 180,000 and change the incidence angle between 0˚ to 12˚. Then, we fix the incidence angle at 2˚ and change the Re from 144,000 to 324,000.

The computational procedure is as follows. The ILES code is used to obtain the time-dependent pressure in the near-field. This is then taken as the input to the FWH code to predict the acoustic far-field. The base flow obtained from the simulation results is taken as the input to the LASTRAC code to predict the growth of disturbances as governed by the linear stability theory. For the ILES code, the present study uses an 1281x789 O-grid, selected based on the grid refinement study detailed in (Golubev et al. 2014). The simulation is run for 720,000 iterations, corresponding to 0.26 seconds of physical time. The far-field acoustic spectra are predicted at 12.5 chords above the trailing edge via the Ffowcs Williams-Hawkings method based on a surface at 5 chords from the airfoil, shown in Figure 3.1. The grid used in the high accuracy simulation is well resolved at this location, having more than 10 points per wavelength. It should be noted that the grid extends to ±100 in both the x and y directions, but is stretched in order to dampen out boundary reflections. Figure 3.1 is cropped to clearly illustrate the location of the control surface. For the LASTRAC code, the boundary layer profiles are generated based on data extracted from the ILES code results, and analysis is carried out for a range of discrete frequencies between 10 Hz and 10,000 Hz.

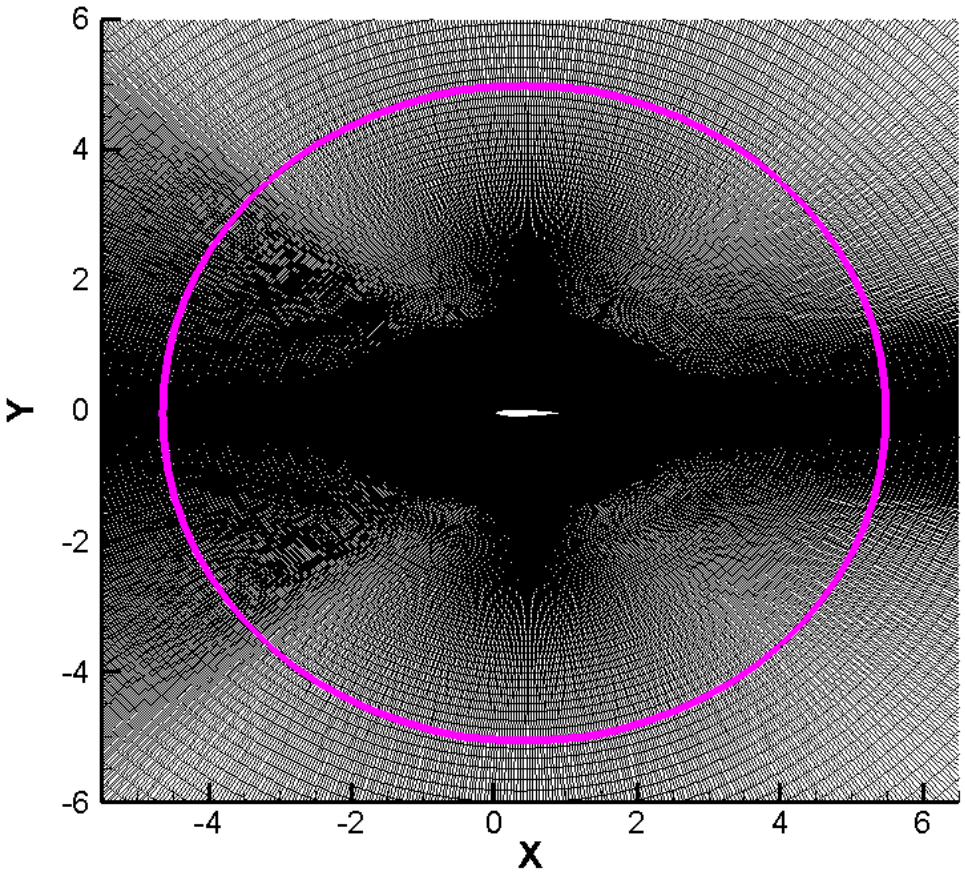

Figure 3.1. Airfoil grid and control surface (purple line).

3.1. Varied Angle of Attack at Re = 180,000

We present here the results at fixed Re of 180,000, but at varied incidence angles. We split the range of incidence angles into what produces tones and what produces tones. This range is indicated by the red line on figure 2.1.

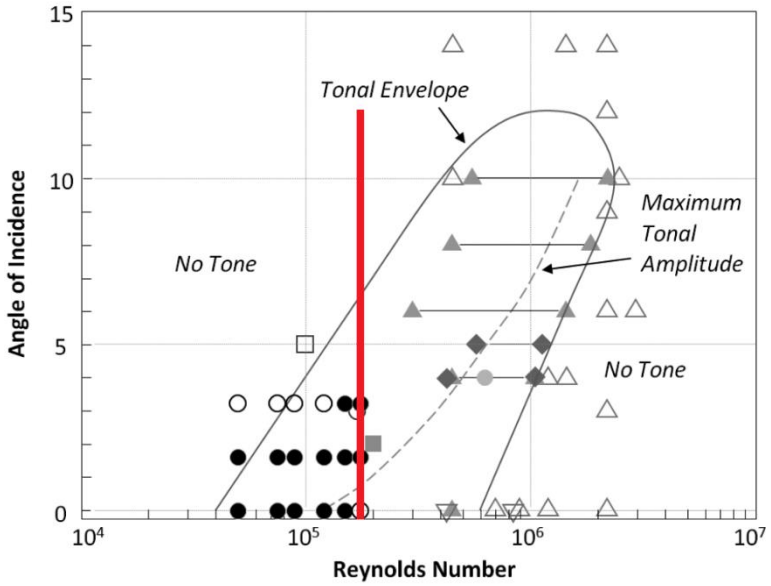

Filled markers represent that a tone was present, while unfilled markers represent that a tone was not present. Data sources: circles (Arcondloulis et al., 2009), triangles (Paterson et al., 1973), inverted triangles (Arbey and Bataille, 1983), squares, (Desquesnes et al., 2007), diamonds (Lowson et al., 1994), Tonal envelope and maximum amplitude line (Lowson et al., 1994).

Figure 3.2. Varying angle of attack for fixed Re = 180,000 (Arcondoulis et al., 2010)

3.1. Tonal cases - Incidence Angle < 6˚.

Based the collected experimental data of tonal observation presented in Figure 3.1 it was expected that tonal noise would be observed starting at 0˚ and continuing as high as 6˚. The far-field acoustic spectrum for each incidence angle is given in Figure 3.3. These far-field spectra were generated for an observer at 12.5 chords above the trailing edge by the Ffowcs Williams-Hawkings method based on a control surface at 5 chord lengths away from the airfoil surface using pressure fluctuation data from the ILES code results

3.1.1. Tones

Clear tonal peaks are observed in the far-field at 0˚, 2˚, and 6˚, and somewhat less

clearly at 4˚. The exact frequencies and intensities of these peaks are listed in Table 2.1.

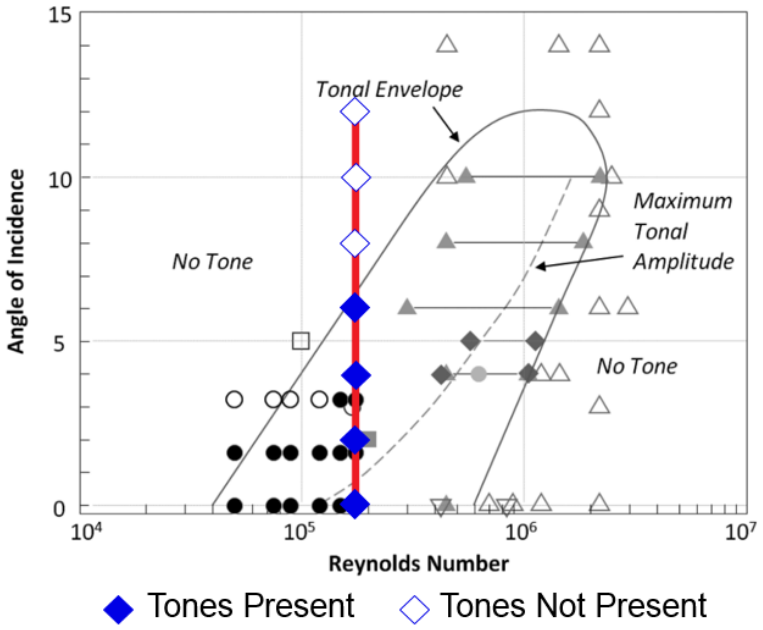

Figure 3.3. Presence of tones for varied angle of attack

For comparison, the near-field spectra are shown as well in Figure 3.4. These spectra are taken directly from the ILES code results at 2 chords above the trailing edge. It can be seen from the 2˚ near-field spectrum that the 2319 Hz tone that appears in the far-field is actually a harmonic of the lower 1156 Hz tone that is the most prominent in the near-field. Therefore, the 1156 Hz frequency will be used for comparison with the stability analysis. For the other cases, the peak tones in the far-field are well matched with the peak tones in the near-field.

Table 3.1. Far-field peak tonal frequencies by case

Angle	Frequency (Hz)	Intensity (dB)
0	1550	95.7
2	2323, 1156	85.1, 79.4
4	1247	85.0
6	1209	90.5

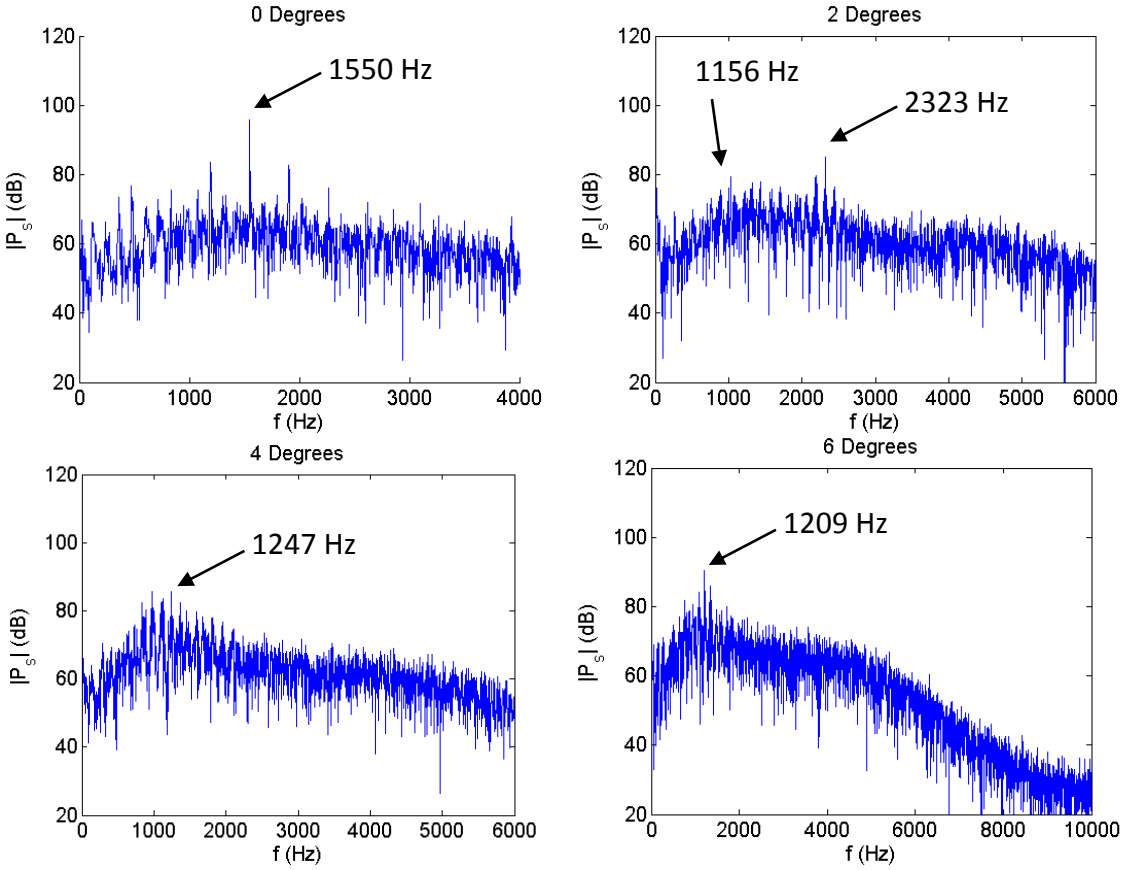

Figure 3.4. Far-field acoustic spectra for cases with tonal peaks at 0°, 2°, 4°, 6°.

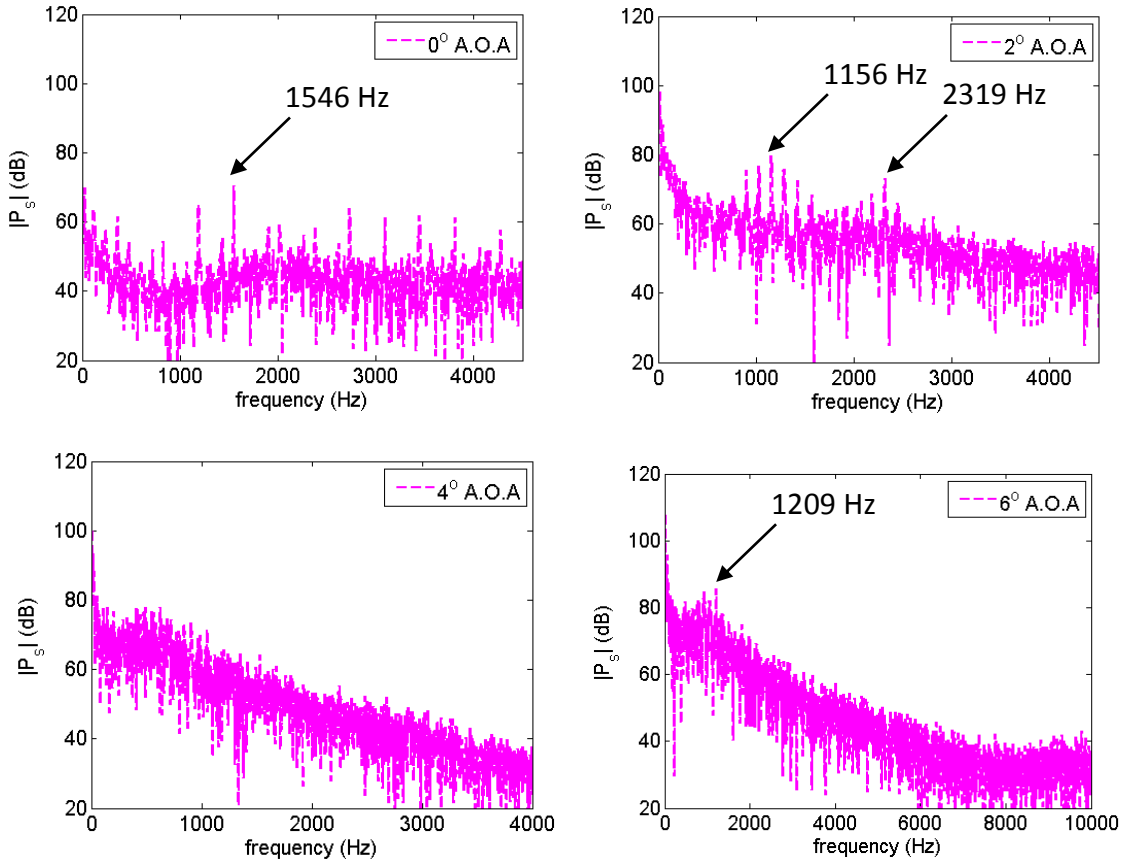

Figure 3.5. Near-field spectra of tonal cases at 0°, 2°, 4°, 6°.

3.1.2. Separation Bubbles

Nash et al. (1999) has highlighted the importance of regions of laminar separation for the amplification of instabilities. Therefore, the coefficient of friction has been calculated along the pressure and suction surfaces of each airfoil in order to identify regions of laminar separation. The coefficient of friction is defined as

$$C_f = \frac{\tau_w}{q_\infty} \tag{3.1}$$

Where τ_w is the wall shear stress

$$\tau_w = \mu \left(\frac{du}{dy}\right)_{y=0} \tag{3.1}$$

Therefore, a location where C_f is negative represents a region of reversed flow in the boundary layer. Table 2.2 lists the exact regions in terms of percent chord, and Figure 3.5 visually illustrates the location on the airfoil surface with a red line. Separation regions exist on both the suction and pressure surfaces for only the 0˚ and 2˚ cases. The suction surface exhibits a separation region for all angles of attack. At 0˚, this region is near the trailing edge and covers approximately 25% of the airfoil. As the angle of attack increases, this region shrinks in length and moves towards the leading edge. The separation region on the pressure surface starts in the same position as that on the suction surface at 0˚, and moves rearward in the 2˚ case. However, the region disappears by 4˚ and does not reappear.

Table 3.2. Locations of suction and pressure side separation bubbles

Angle	Suction Side	Pressure Side
0°	70% - 96%	70% - 96%
2°	53% - 73%	82% - 100%
4°	35% - 48%	No Separation
6°	9% - 25%	No Separation

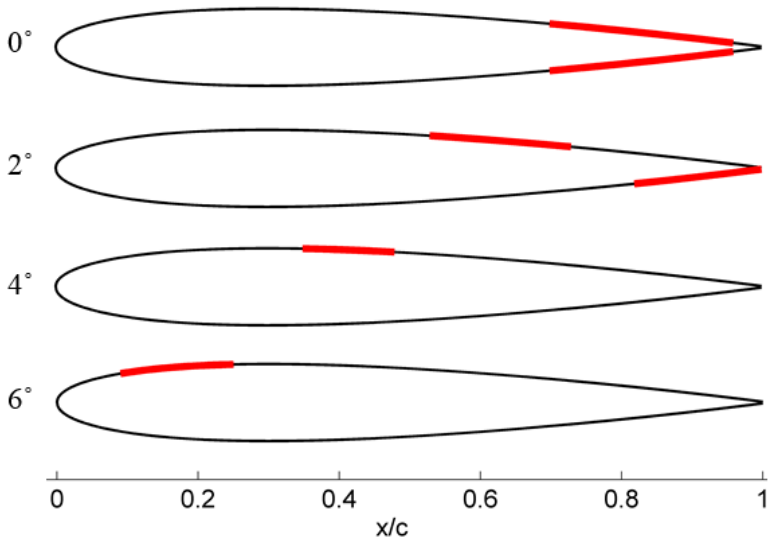

Figure 3.6. Separation regions for tonal cases.

3.1.3. Linear Stability

For the 0˚ case, stability analysis was conducted for frequencies ranging from 0 to 4000 Hz by increments of 10 Hz, and the peak frequency is calculated. Since this case is symmetric, only the data for the suction surface are shown. The chordwise behavior of the instability growth can be seen in Figure 3.6. The primary region of instability growth corresponds very well with the location of the laminar separation region, as indicated by the dashed blue lines. These mark the beginning and end of the separation region, determined from the coefficient of friction plot shown in the bottom of Figure 3.6. The presence of these separation regions can also be seen in the velocity contours, in which the thick blue regions indicate that the average flow velocity is less than or equal to 0 m/s.

As with the 0˚ case, it can be seen from Figure 3.7 for incidence angle of 2° that the regions of predicted instability growth correspond with the locations of the separation regions. It is also clear that the growth in RMS pressure is correlated with location of

instability amplification.

For 6˚, only results for the suction side are shown since there is no amplification on the pressure side. Additionally, the amplification of the frequency of the acoustic tone is plotted for comparison. Figure 3.9 shows that although the 6375 Hz peak frequency predicted by stability analysis theoretically reaches a much higher amplification than the observed tonal peak of 1205 Hz. It is not unstable past 20% chord and will likely be damped out. The lower frequencies, although they do not reach the same amplification, remain unstable the entire length of the airfoil. This is further described in Section 3.1.4. It is thus clear that the rapid growth of disturbance is associated with the presence of a separation region. The reason is that for the attached region the instability waves are the T-S waves associated with the viscous effects. For the separation region, the stability is that of the K-H type associated with velocity gradients.

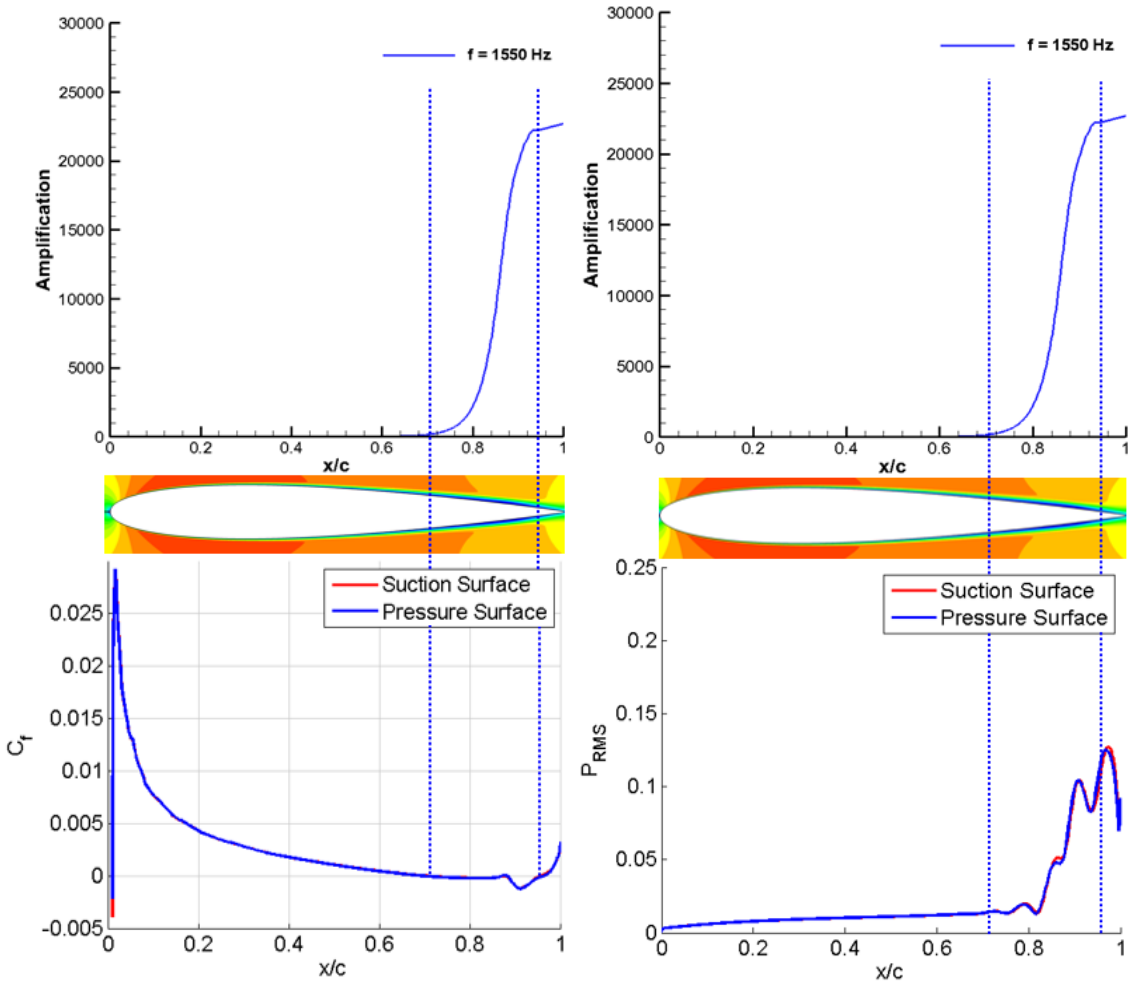

Figure 3.7. Chordwise amplification of predicted peak for 0˚.

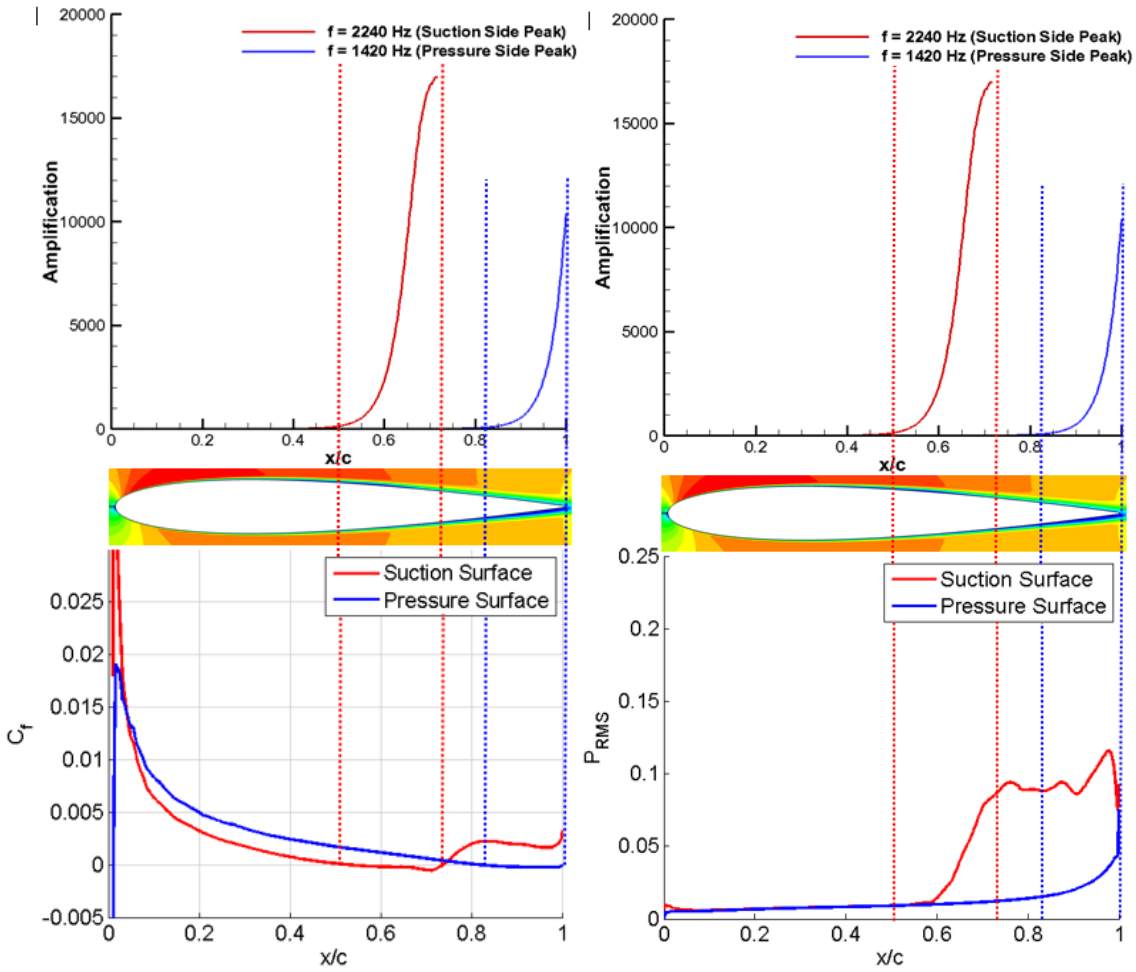

Figure 3.8. Chordwise amplification and boundary layer statistics for 2˚

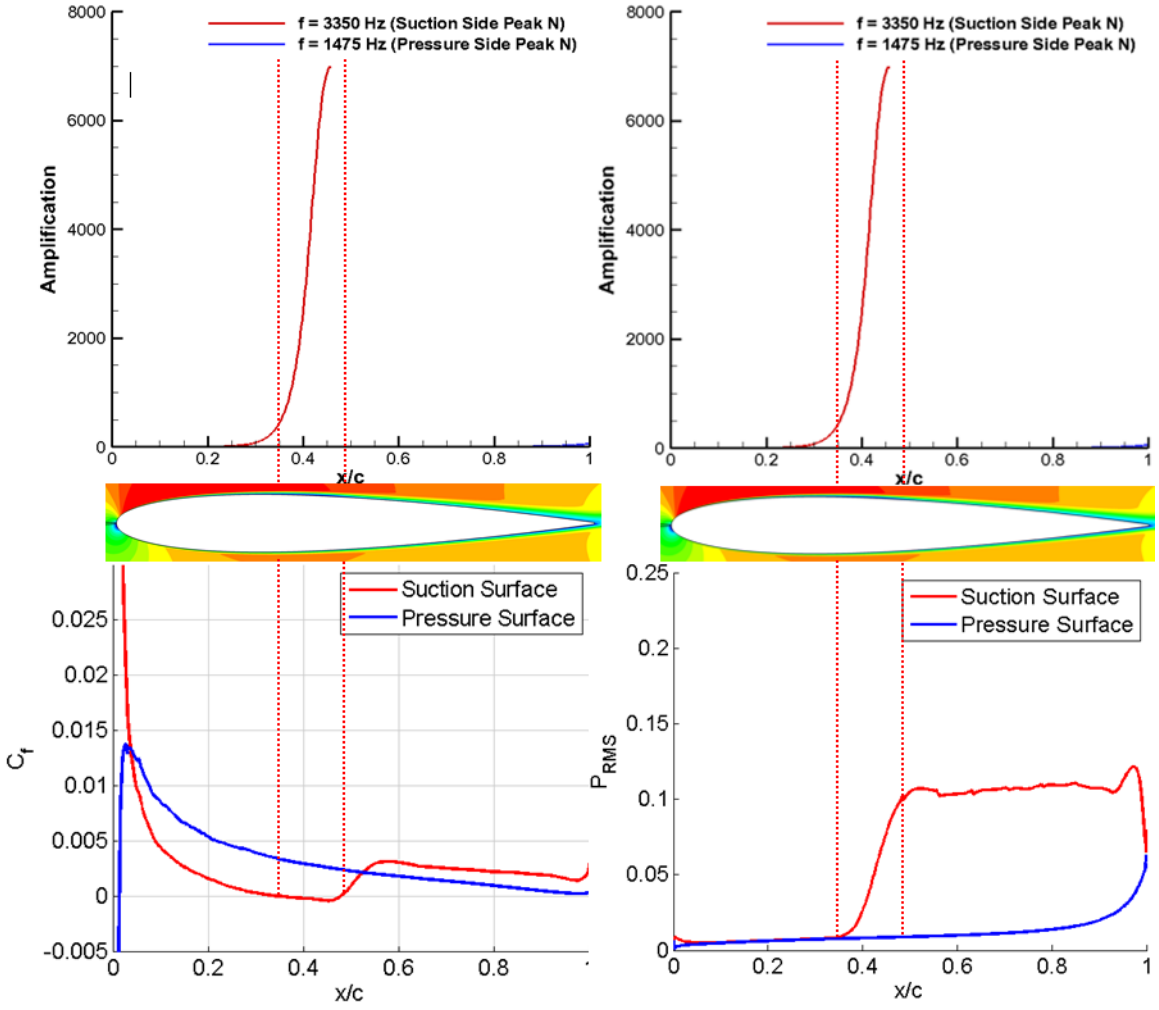

Figure 3.9. Chordwise amplification and boundary layer statistics for 4˚

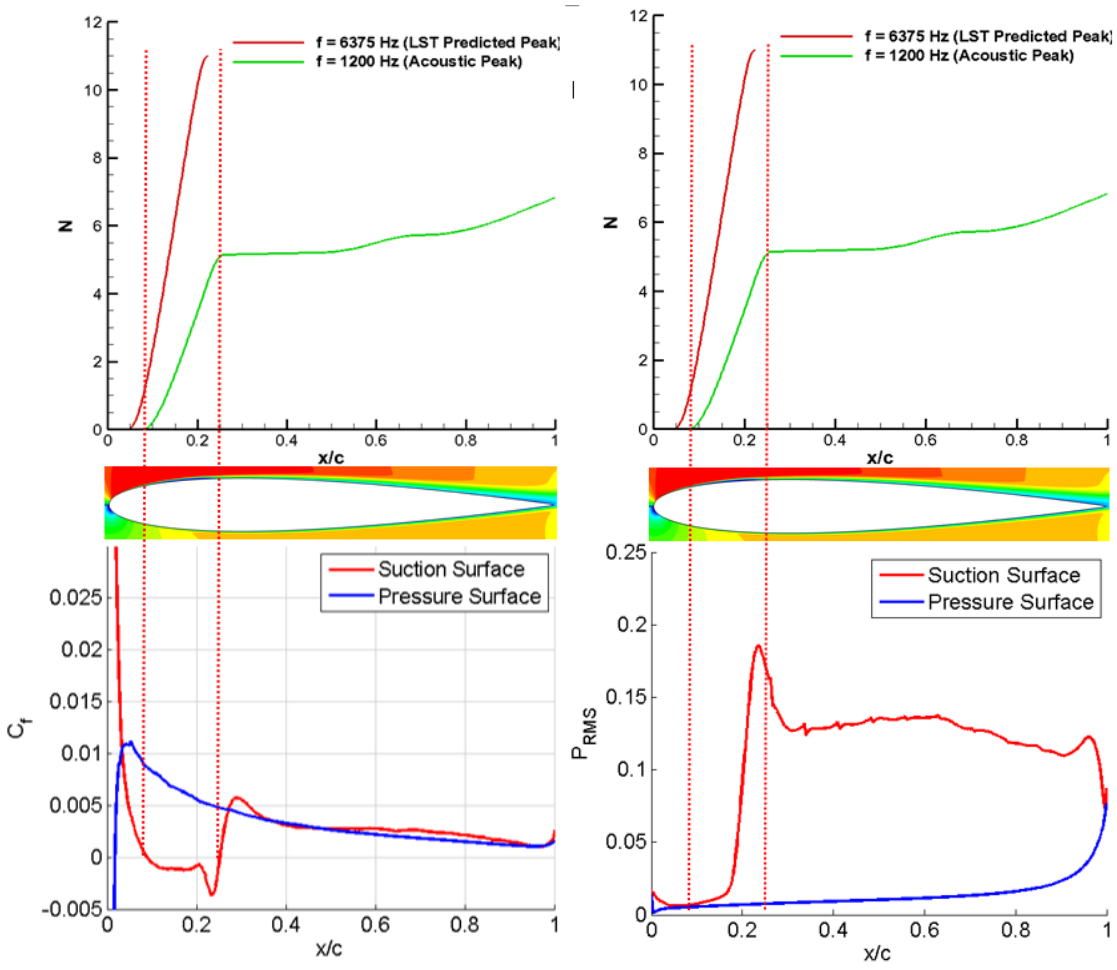

Figure 3.10. Chordwise amplification and boundary layer statistics for 6˚.

3.1.4. Correlation Between Acoustic Tones and LST Peaks

Having calculated the amplification rates for various frequencies, the predictions of linear stability theory are compared with the observed tonal frequencies in order to determine how they correlate. Figure 3.11 through Figure 3.14 show the maximum amplification reached for all frequencies for angles 0°, 2°, 4°, and 6° respectively. In these figures, the blue solid blue line is the maximum amplification reached for each frequency as indicated on the left axis, and the solid green line is the chordwise location

at which the maximum amplification is reached. The dashed blue line indicates frequency for which the highest amplification is observed. For the 0° case, the peak frequency predicted by stability analysis is 1500 Hz, shown by the dashed black line. At 0˚ value most highly amplified predicted frequency agrees very well with the observed far-field frequency of 1550 Hz, having an error of only 3.2%. For the 2˚ case, there is a difference of several hundred Hz between the predicted peak amplifications for the suction and pressure surfaces. The near-field tonal frequency of 1156 Hz does not agree with the peak frequencies predicted LST for either the suction or the pressure surface. However, it is a highly amplified frequency on both surfaces. The same trend is observed for the 4˚ case with the exception that instability growth is very weak on the pressure surface due to the absence of a separation region.

At 6˚, there is no longer any disturbance growth on the pressure side due to the favorable pressure gradient induced by the higher angle of attack. Therefore, only results for the suction side are shown for these cases. The predicted peak of 6375 Hz on the suction side is drastically different from the observed far-field tonal peak of 1209 Hz. However, it can be noted from the green line in Figure 3.13 that the tonal peak does fall within the range of frequencies that remain unstable all the way to the trailing edge. As the angle of incidence increases, the disparity between these values grows larger. Possible reasons for these disagreements are discussed in Section 3.1.5.

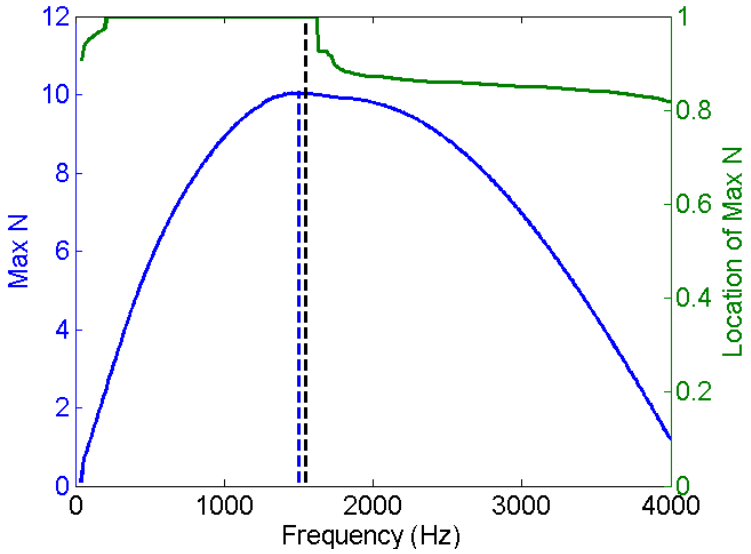

Figure 3.11. 0˚ Amplification.

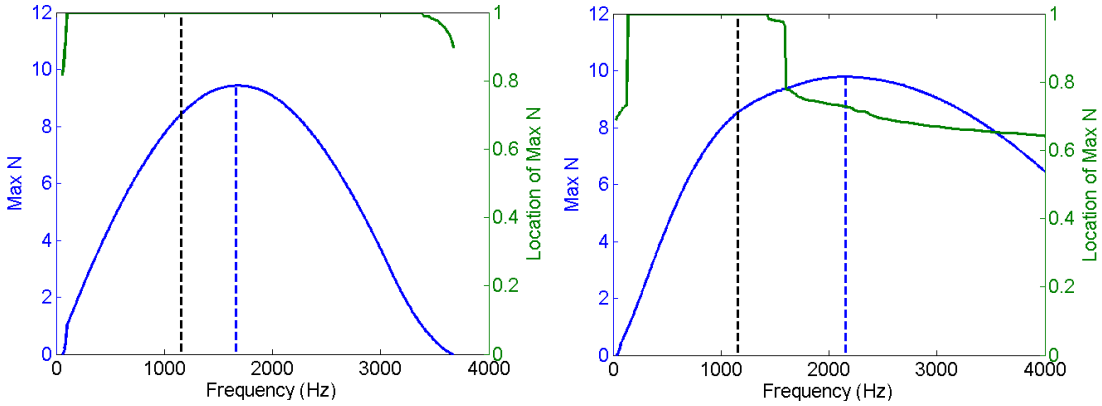

Figure 3.12. 2˚ Amplification (pressure surface left, suction surface right).

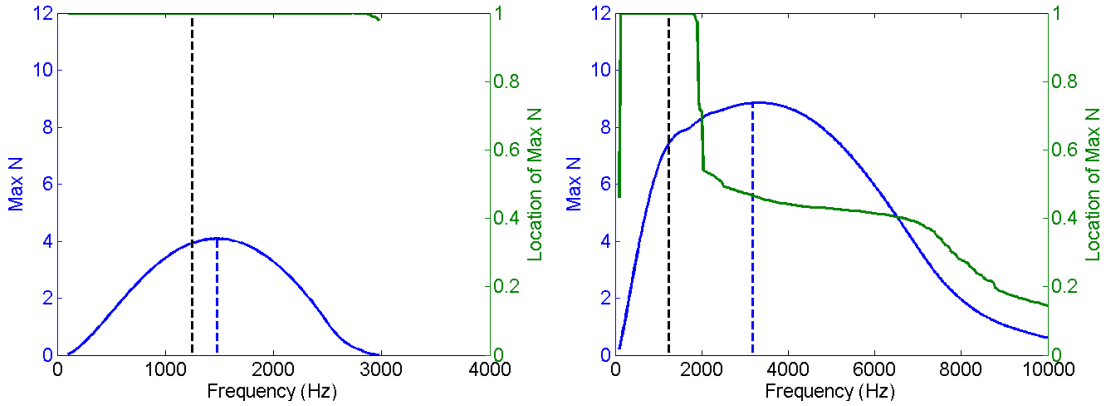

Figure 3.13. 4˚ Amplification (pressure surface left, suction surface right).

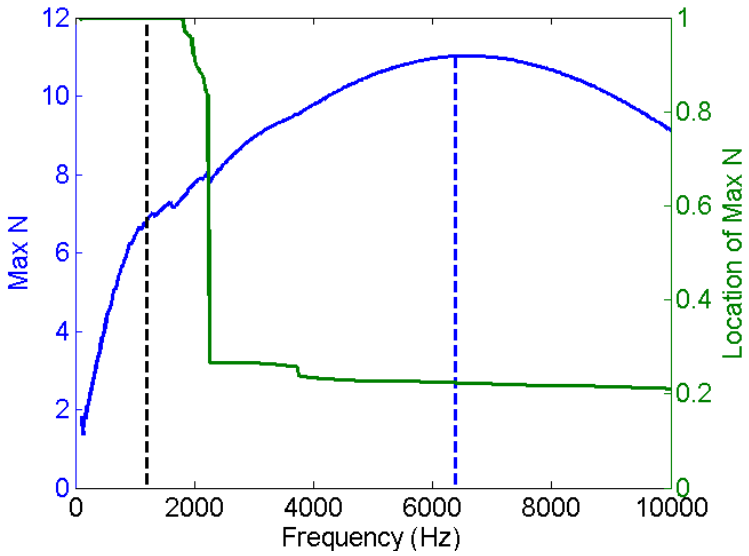

Figure 3.14. 6˚ Suction Surface Amplification.

Figure 3.14 shows the maximum amplification reached at the TE for both the suction and pressure surface at all angles. For the pressure surface, the amplification at the TE rapidly drops to 0 as angle increases due to the disappearance of the separation region, while amplification is still observed on the suction surface for all angles to some extent.

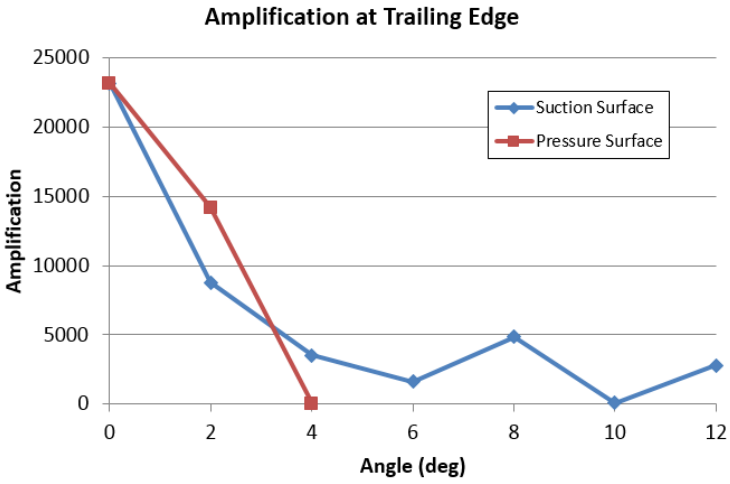

Figure 3.15. Maximum amplification at the trailing edge.

3.1.5. Vortex Shedding

Since the frequency of the most amplified instability wave does not coincide with tone frequency, let us examine the vortex-shedding frequency to determine if they correlate with the acoustic frequency. The formation of vortex shedding is demonstrated in the vorticity contours in Figure 3.15, which clearly illustrates the roll-up of instabilities into vortices, originating from the separation regions on each surface. These vortices are prominent on both surfaces at 0˚ due to the flow symmetry, but vortices are not distinguishable on the pressure surface for 2°, 4°, or 6°. It also appears that the pattern of vortices remains fairly regular to the trailing edge up to 6˚.

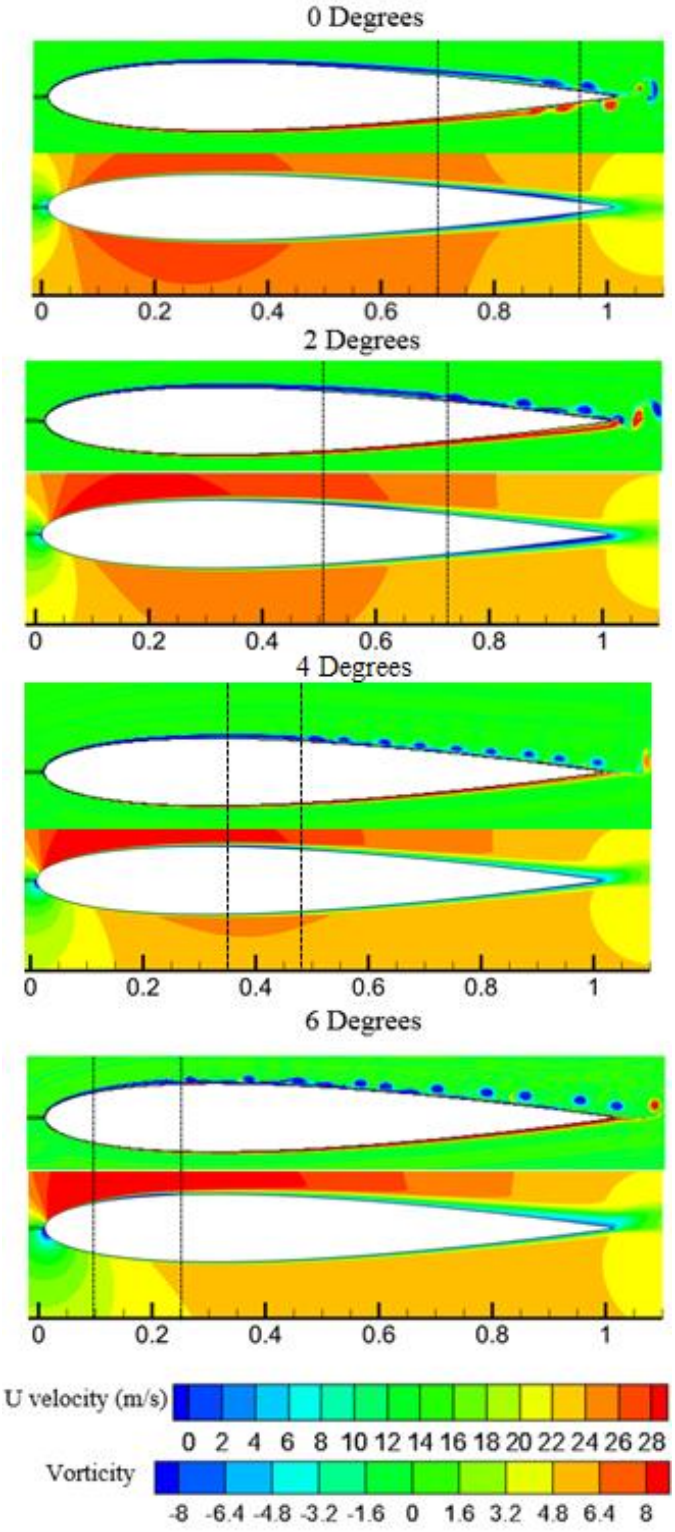

Figure 3.16. Instantaneous vorticity contours compared to time averaged velocity.

The vortex shedding frequency for each angle was extracted from visual inspection of the ILES code results compiled into movies of the pressure contours at the trailing edge, covering 7.3% (0.019 s) of the total simulation time (0.26 s). An example of such contours is shown in Figure 3.16.

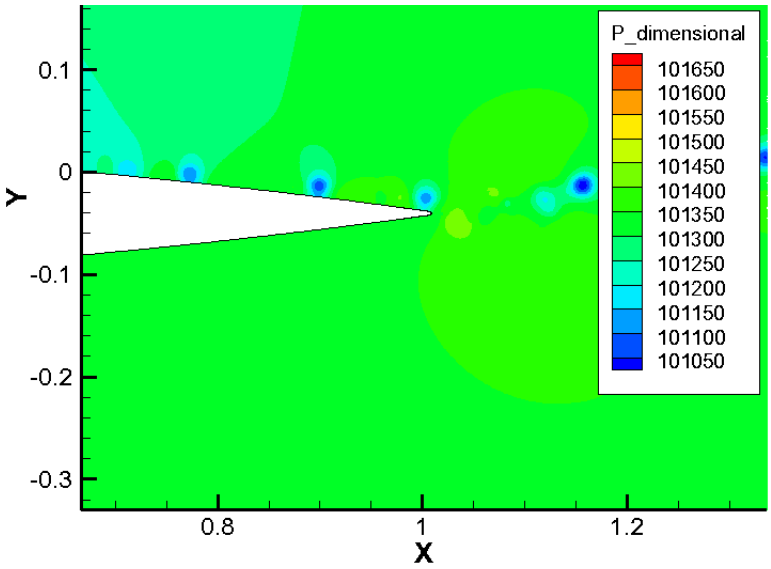

Figure 3.17. 2˚ pressure contour used to calculate vortex shedding frequency.

This inspection showed that the vortex shedding frequencies agree with the observed tonal frequencies within 2 percent error. Therefore, it can be reasonably concluded that the observed tones correspond with the vortex shedding frequency, with acoustic waves generated as the vortices are convected past the trailing edge of the airfoil. The close correlation between acoustic tones and the vortex shedding frequency can be seen in Figure 3.17. It also illustrates the disparity between the acoustic tones and the most amplified instability predicted at the trailing edge. These results are comparable to those of Jones and Sandberg (2011). They performed stability analysis based on 2D DNS simulations of a NACA0012 airfoil at Re = 10,000 at 0˚ and 0.5˚, and found that the

acoustic tone was identical to the vortex shedding frequency, but was of lower frequency than the most amplified frequency predicted by LST.

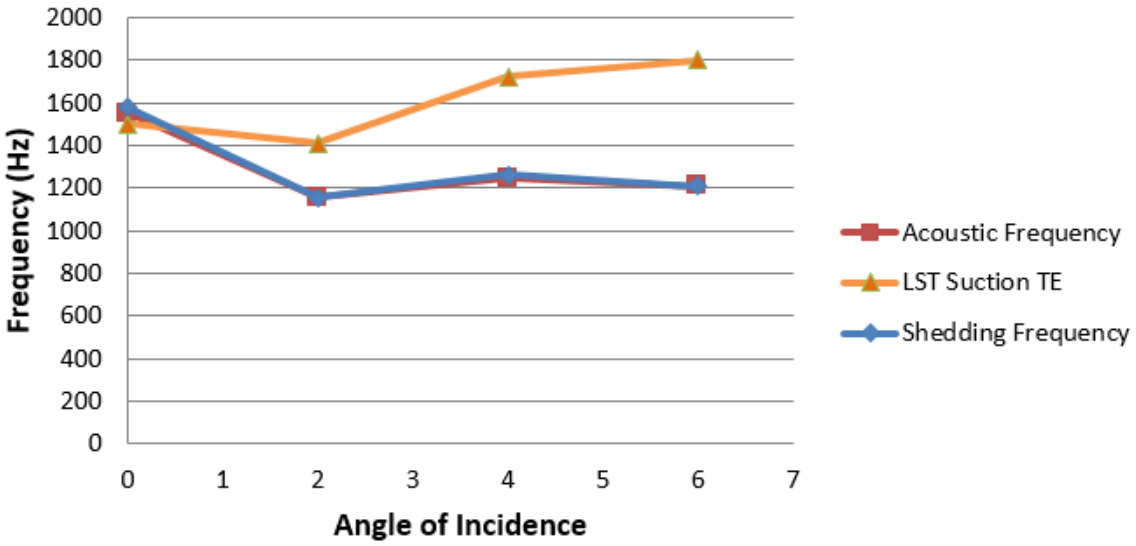

Figure 3.18. Correlation between observed and predicted frequencies

3.1.6. Correlation with the Airfoil Surface Pressure

The acoustic frequency is reflected in the surface pressure spectra as well. Figures 3.19 and 3.20 shows that the frequency observed in the far-field is also present in the wall pressure spectra. The wall pressure spectra for 2˚, shown in Figure 3.20, reveals that the same peak frequencies of the pressure fluctuations are seen on both surfaces. However, amplitudes are significantly higher on the suction surface, indicating that the instabilities on this surface are the dominant source of the fluctuation growth.

At 4° and 6˚, the frequency appear to be selected based on their sustained instability all the way to the trailing edge. Linear stability results suggest that higher frequencies should be more highly amplified early on the airfoil surface at this angle, yet the same frequency is dominant at all positions. The presence of this peak frequency at

all points on the airfoil surface indicates that this frequency has been selected and reinforced via the acoustic feedback loop.

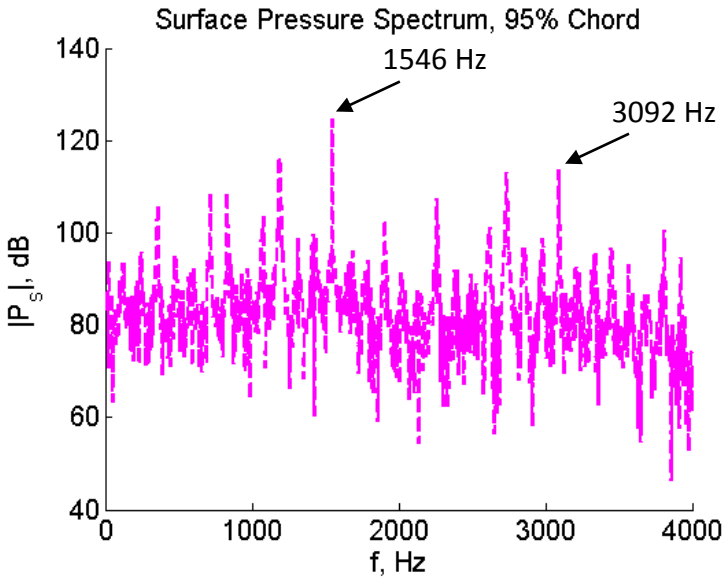

Figure 3.19. 0° Surface pressure spectra.

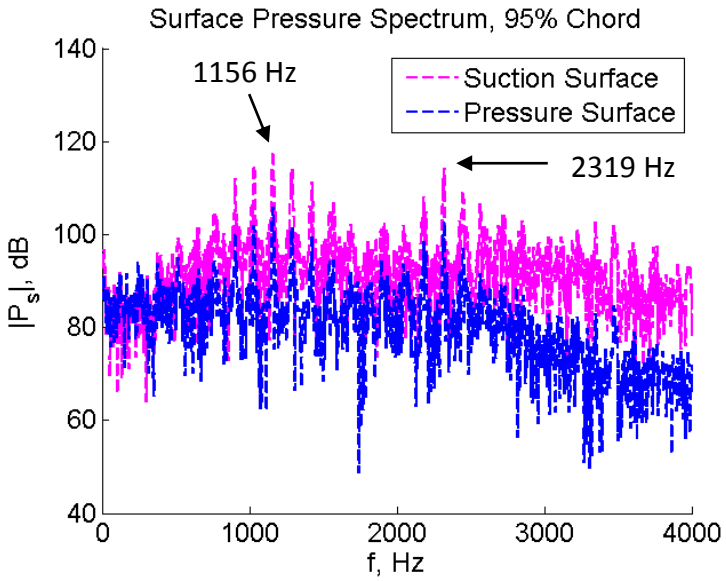

Figure 3.20. 2˚ Surface pressure spectra.

At 4° and 6˚, the frequency appear to be selected based on their sustained instability all the way to the trailing edge. Linear stability results suggest that higher frequencies should be more highly amplified early on the airfoil surface at this angle, yet the same frequency is dominant at all positions. The presence of this peak frequency at all points on the airfoil surface indicates that this frequency has been selected and reinforced via the acoustic feedback loop. This trend is clearer at 6° in Figure 3.22, but is still observable at 4° in Figure 3.21.

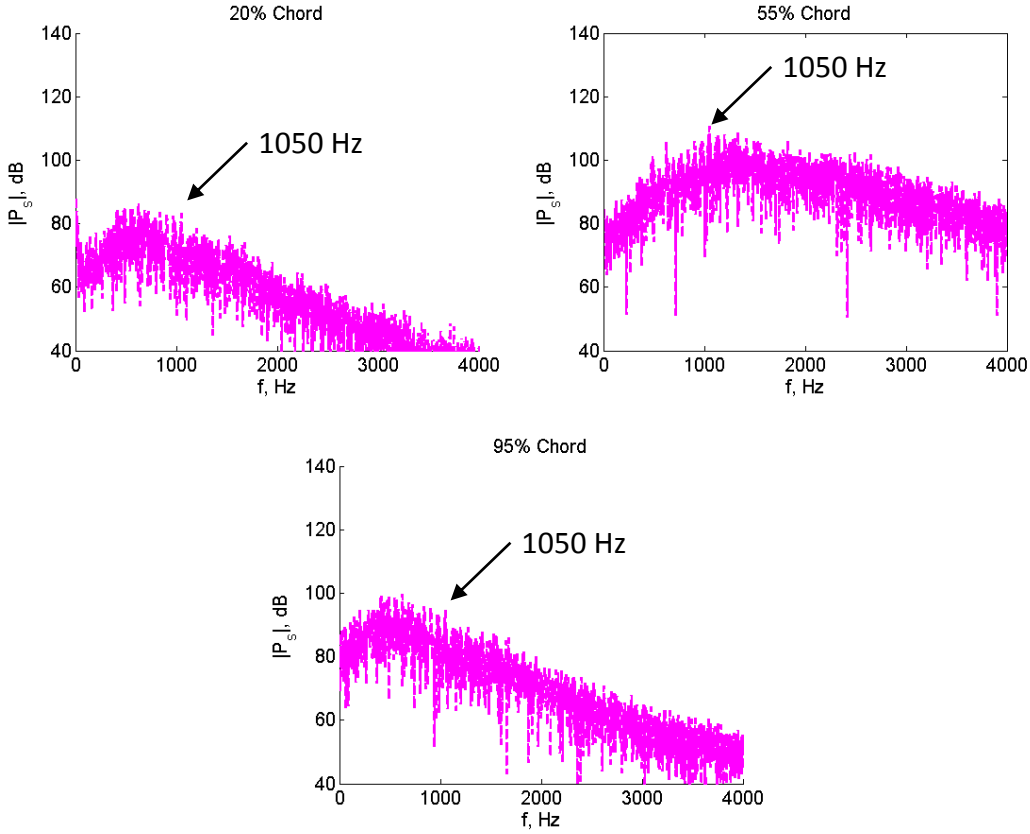

Figure 3.21. Suction surface wall pressure spectra at 4˚.

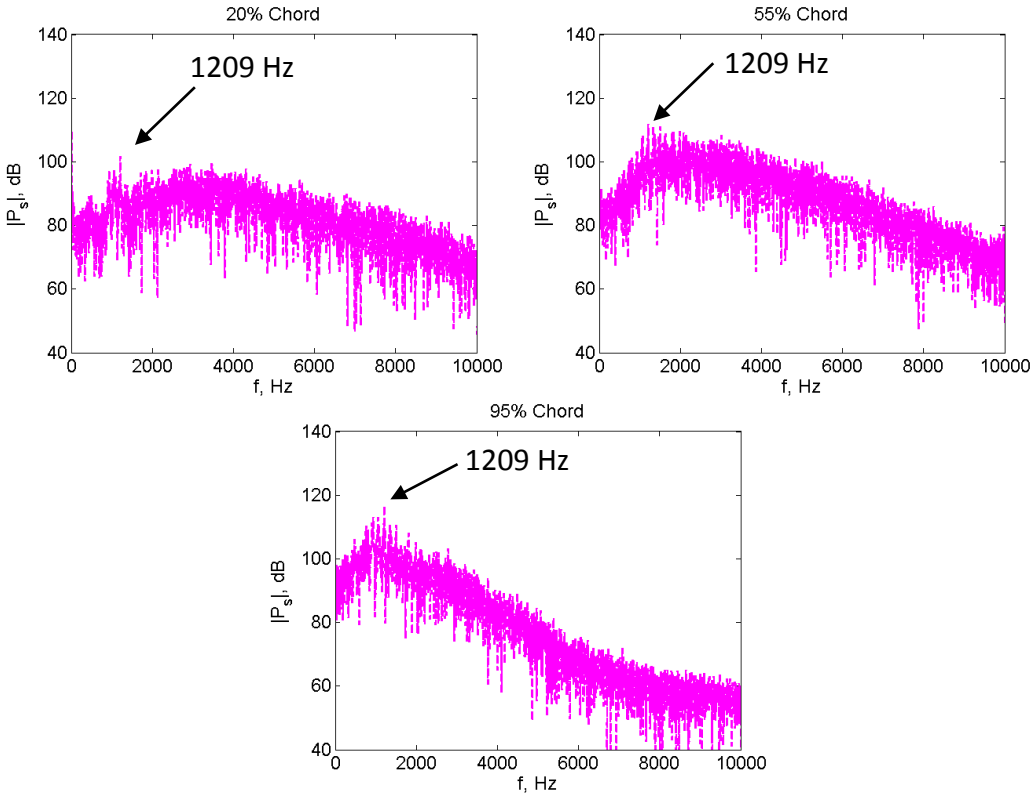

Figure 3.22. Suction surface wall pressure spectra at 6˚.

3.1.7. The Proposed Feedback Loop

Based on the results so far, we can make the following comments on the mechanism for the tone generation. These findings are discussed in the context of the feedback loop, which can be essential described in 4 parts, as listed below:

1. Initial instability growth takes place with rapid amplification of instabilities within the separated shear layer in the separation regions, where the instabilities roll up into vortices.
    a. Flow separation is a necessary, but not sufficient, condition for the generation of tones. Nash et al. had proposed that in order for tonal noise to be present, a region of separated or inflectional flow must

exist near the trailing edge on the pressure side. The present study indicates, however, that tonal noise may still be expected when there exists a separation region as far forward as 25 % on the suction surface at small incidence angles.

b. Separation changes the nature of the instability modes from that of the slowly-growing TS waves associated with attached laminar BL to that of rapidly-growing KH instability associates with mean flow velocity gradient (as shown in Figure 3.6 through Figure 3.9). This explains the rapid increase in the RMS of the surface pressure predicted by the high accuracy simulation at the separation location.

c. The LST predicts a certain peak frequency for maximum growth. However, in determining this peak frequency, it is assumed that the initial amplitudes of all frequency components are identical. This peak frequency could change if the initial level of disturbance is not uniform and is a function of the frequency

2. As the vortices pass the trailing edge of the airfoil, they create a scattered acoustic field.

   a. In all cases, the tonal acoustic frequency coincides with the peak frequency of the surface pressure and with the vortex shedding frequency (Figure 3.17), as was observed by Nash et al. (1999).

   b. The LST predicts a wide spectrum of rapidly growing flow waves; these waves scatter at the trailing edge and generate acoustic waves. The strength of the scattered acoustic waves relative to the incident

fluid waves decreases with increasing frequency, as postulated by Jones and Sandberg (2011) based on their application of Amiet's (1976) theory of trailing edge noise. Therefore, the peak frequency of the max scattered wave is less than the peak frequency for max LST growth because the process of TE scattering is more efficient at lower frequencies.

3. Acoustic waves propagate upstream.
4. The acoustic waves, through BL receptivity, selectively amplify certain frequencies on the airfoil surface.
    a. As a result of the BL receptivity process, the acoustic waves excite some frequency disturbances more than the others. Thus, the initial level of disturbance available to be amplified by the LST is not uniform and is a function of the frequency. Jones and Sandberg (2010) found that the receptivity process, like the TE scattering process, becomes increasingly efficient at lower frequencies. This results in locking a certain frequency for optimum acoustic generation.

It appears that linear stability alone cannot explain the mechanism of frequency selection within the feedback loop, but that the selection mechanism may be a complex interaction that depends upon the TE scattering and BL receptivity processes.

3.2. Non-tonal cases

3.2.1. Acoustic-Spectra

As expected, no tonal peaks are observed at 8˚, 10˚, or 12˚, whose spectra are given in Figure 3.20. Only broadband trends are observed at these angles.

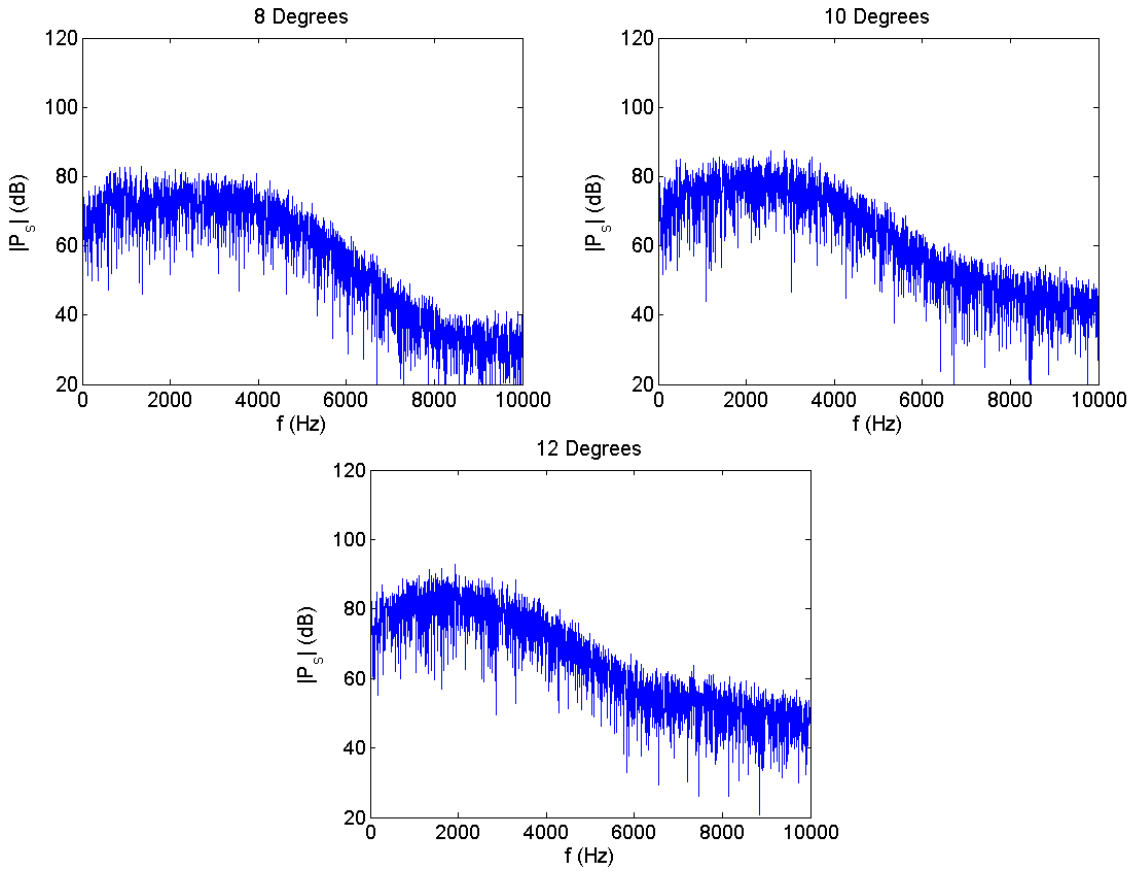

Figure 3.23. Far-field acoustic spectra for cases without tonal peaks.

3.2.2. Flow Separation

No separation regions are observed on the pressure surface at 8˚, 10˚, or 12˚. However, compact regions of separation continue to persist on the suction surface very close to the leading edge, as indicated by the coefficient of friction. At these high angles, the C_f near the trailing edge on the suction surface begins to approach 0, indicating that

the flow at the trailing edge is becoming highly unsteady due to the strengthening adverse pressure gradient as a result of the increased angle of attack. At 10˚, the C_f is close to zero at approximately the last 30% of the airfoil.

Table 3.3. Locations of suction and pressure side separation bubbles

Angle	Suction Side	Pressure Side
8	3% - 12%	-
10	2% - 10%	-
12	2% - 8%	-

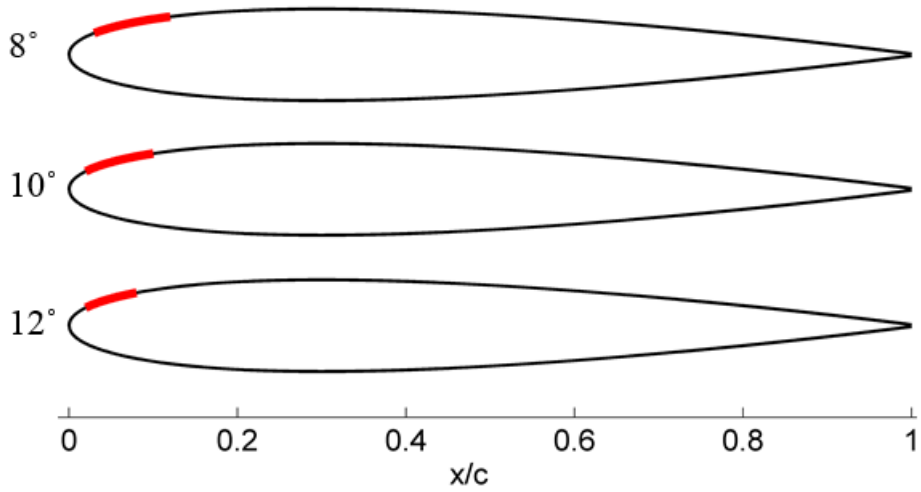

Figure 3.24. Separation regions for cases without tones.

3.2.3. The LST Results

The stability results exhibit the same trends between 8˚ and 12˚. Since no tones are observed in these cases, the lines plotted in Figure 3.22 through Figure 3.24 are chosen arbitrarily to represent the behavior of a range of frequencies.

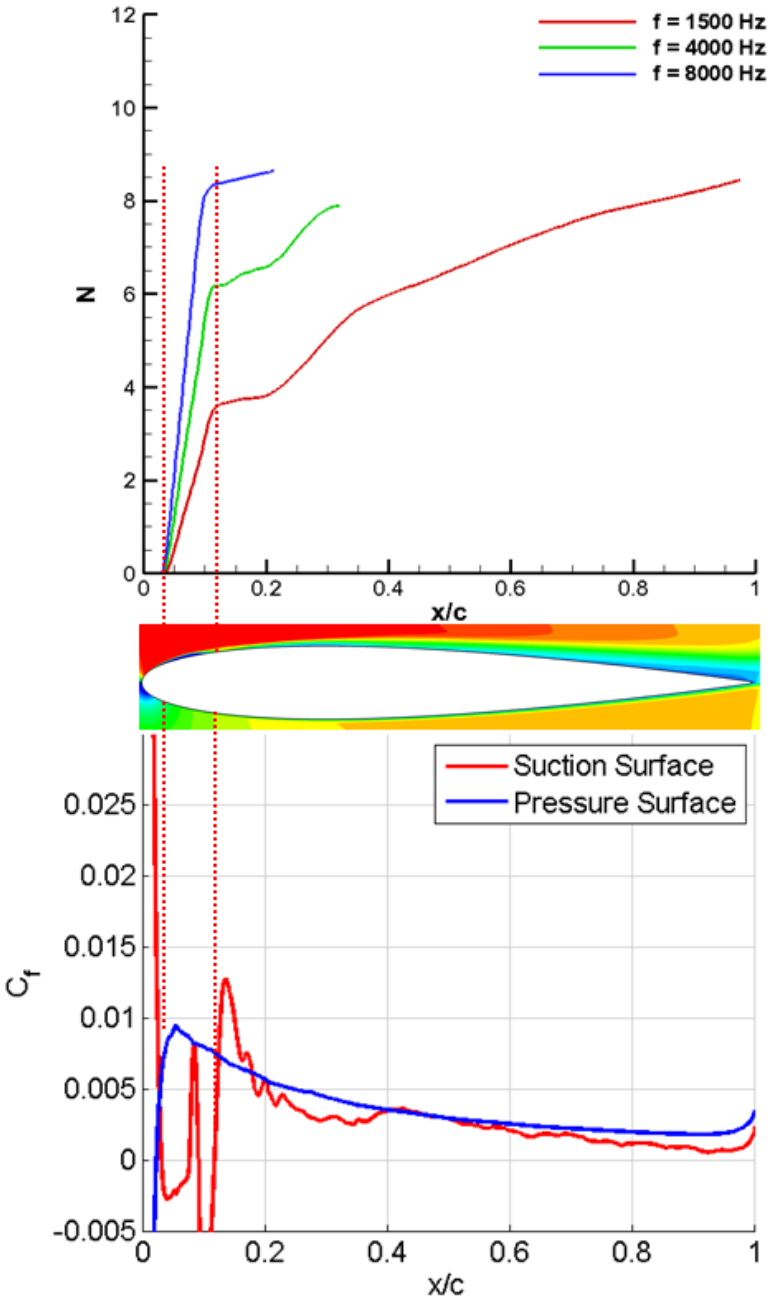

Figure 3.25. Chordwise amplification of predicted frequencies for 8˚

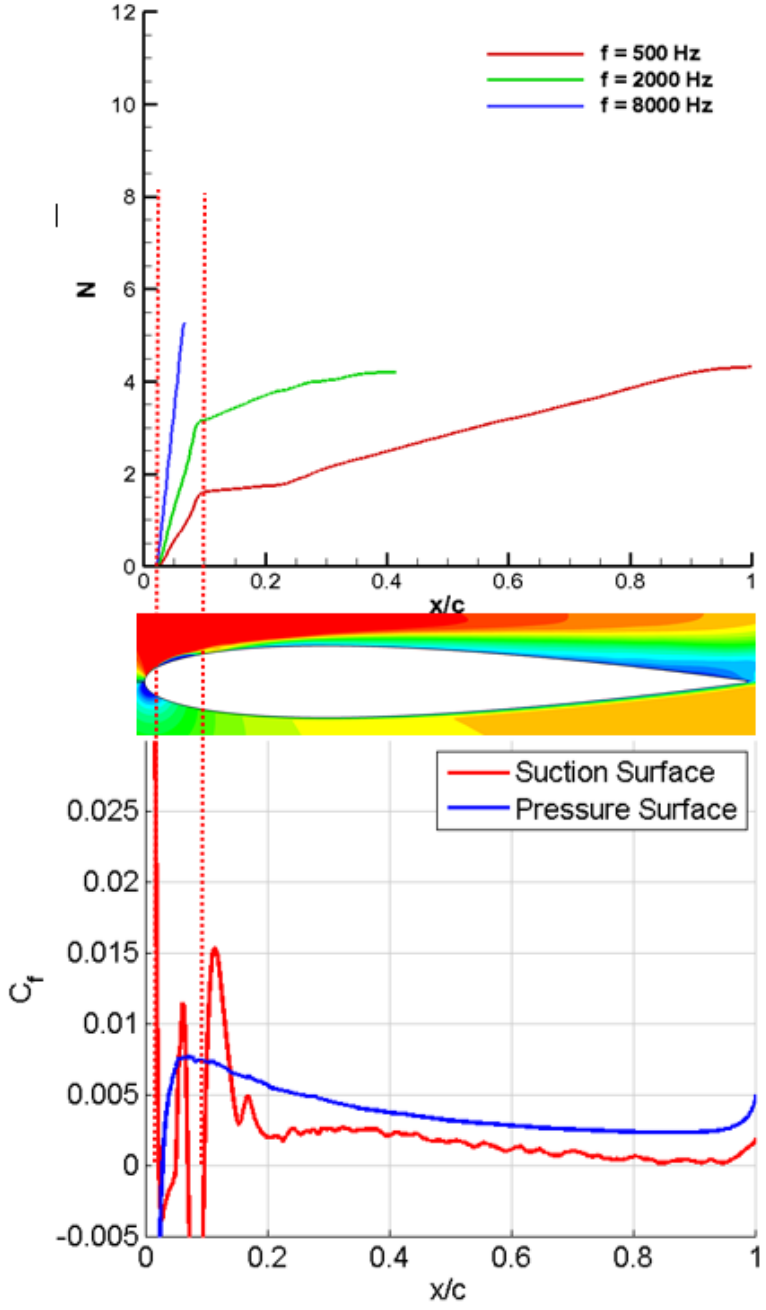

Figure 3.26. Chordwise amplification of predicted frequencies for 10˚

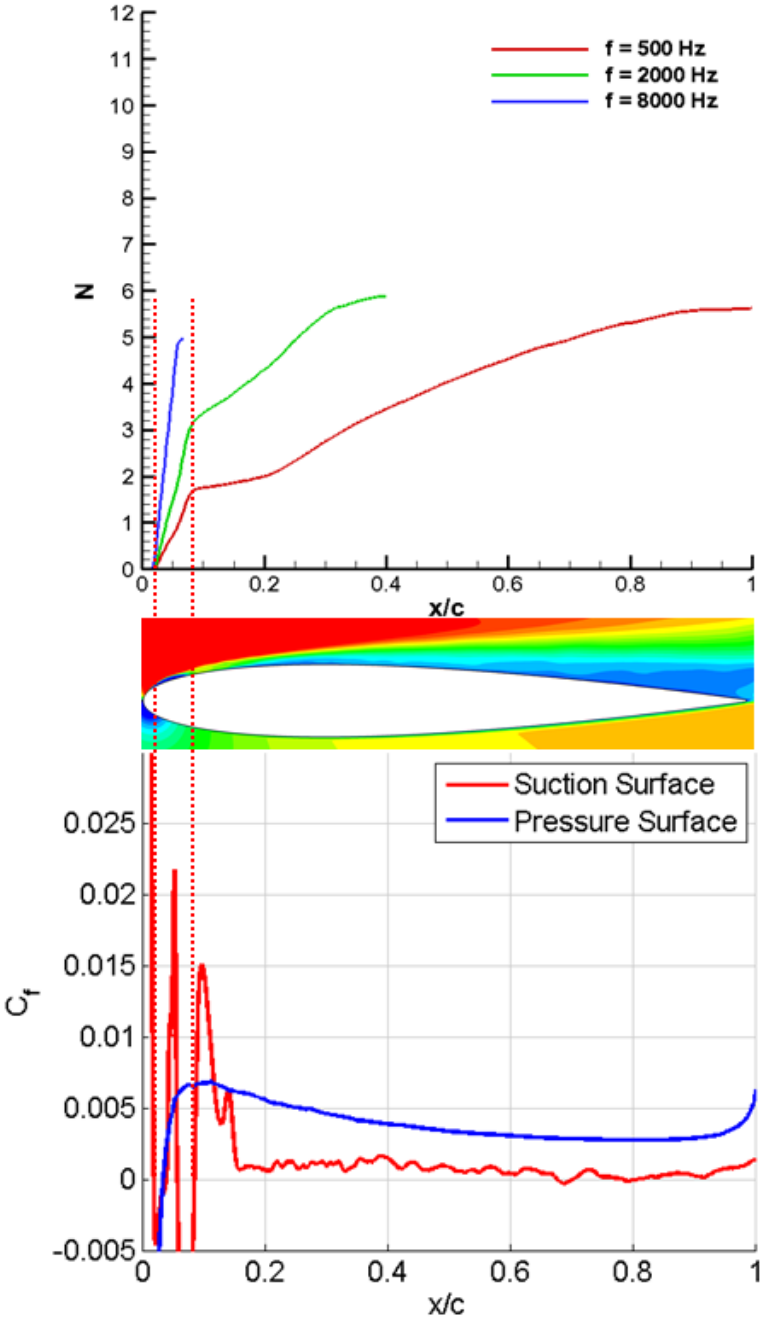

Figure 3.27. Chordwise amplification of predicted frequencies for 12˚

Figure 3.23 shows that high frequencies are amplified near the leading edge, but do not survive further downstream, while lower frequencies continue to grow along the full chord length. There is a notable change in the shape of the N vs. Frequency plots

between the tonal and non-tonal cases. While the lower angle cases showed somewhat parabolic distributions with a single peak, Figure 3.25 through Figure 3.27 show that at for the non-tonal cases, all frequencies are amplified to similar levels with a relatively chaotic trend as frequency increases.

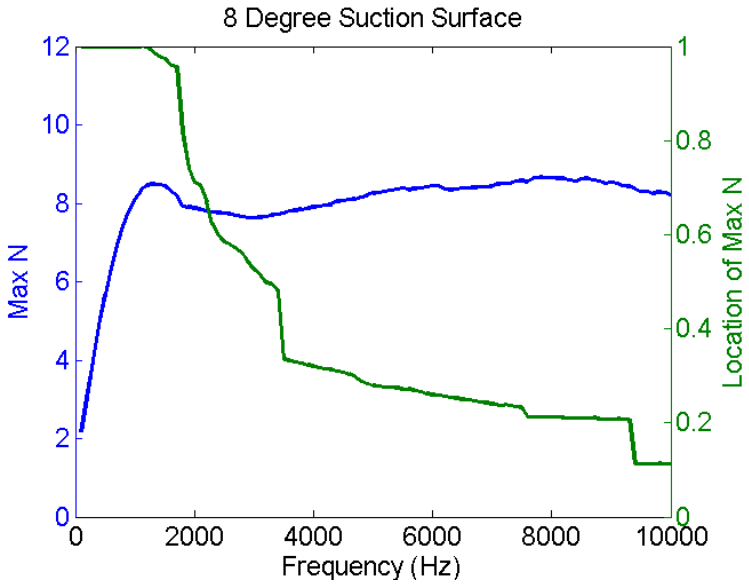

Figure 3.28. 8˚ Amplification

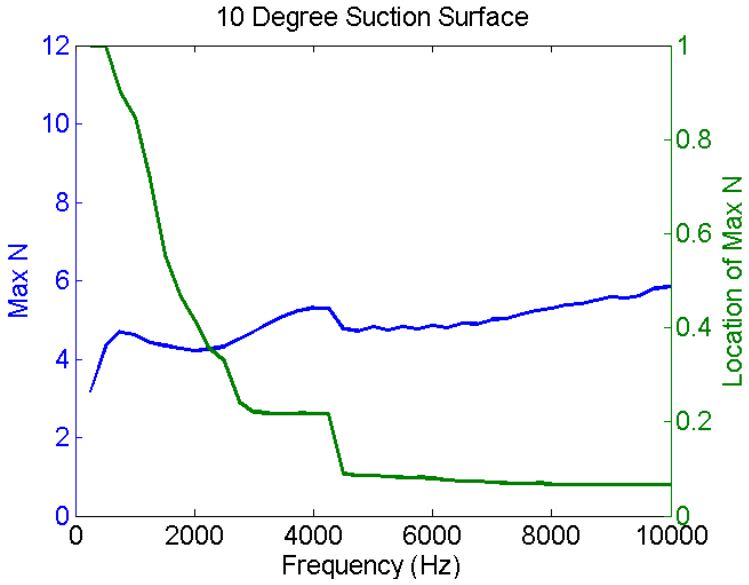

Figure 3.29. 10˚ Amplification

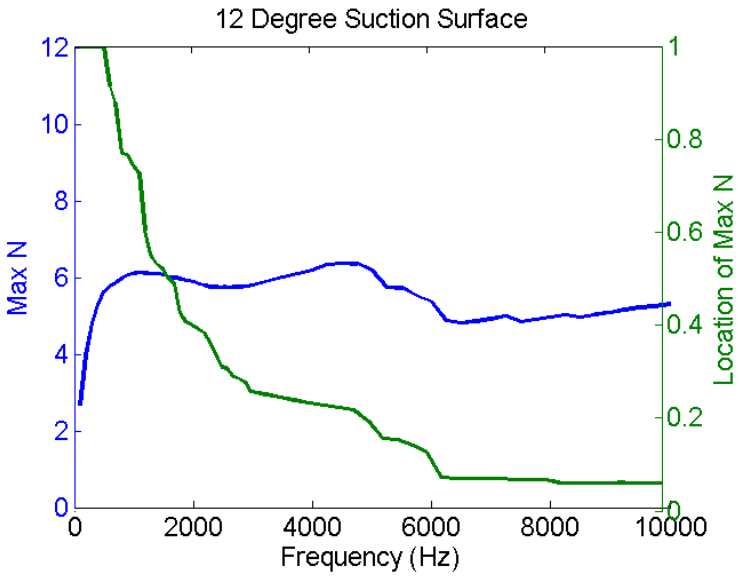

Figure 3.30. 12˚ Amplification

3.2.4. Vorticity

The change in the nature of the amplification behavior between is corroborated by the vorticity contours in Figure 3.28. These contours show that at 8˚, the unsteadiness of the flow approaching the trailing edge causes the pattern of vortices to become less regular and drift upwards from the surface as they move downstream. Additionally, it can be seen that at 8˚, 10˚, and 12˚, rather than the orderly formation of uniform vortices seen at the lower angles, the small scale turbulence appears to develop near the leading edge. As angle of attack increases, the unsteadiness of the flow at the trailing edge and the development of turbulence near the leading edge seem to be the primary cause of the cessation of the tones.

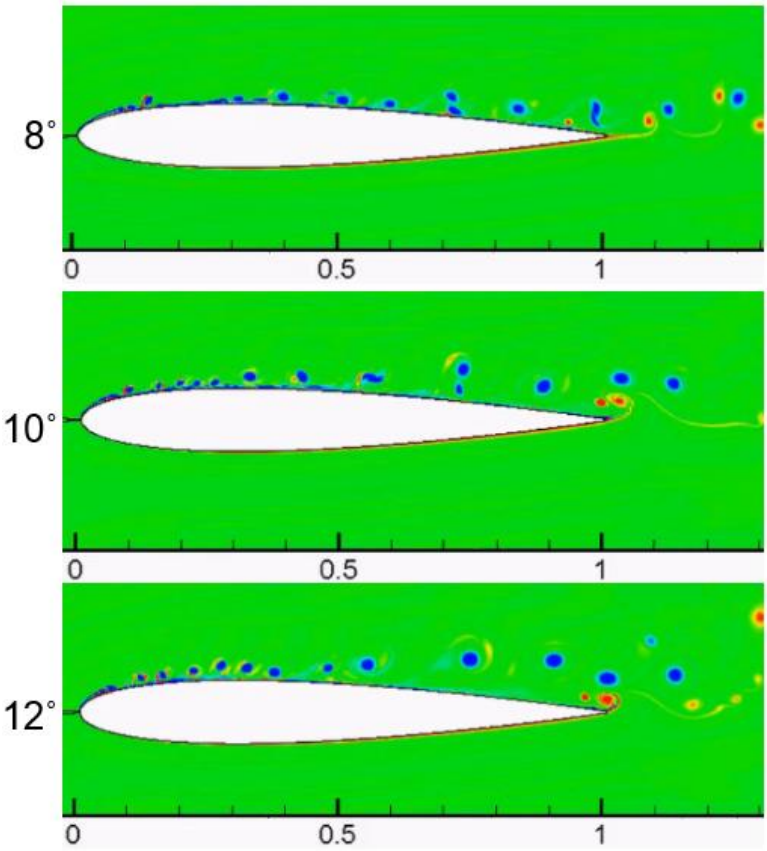

Figure 3.31. Instantaneous vorticity contours.

3.2.5. Surface Pressure Spectra

In contrast to the 6˚ case, Figure 3.29 shows that in the 10˚ case where no tones are observed, no consistent peak frequency exists at all points in the wall pressure spectra.

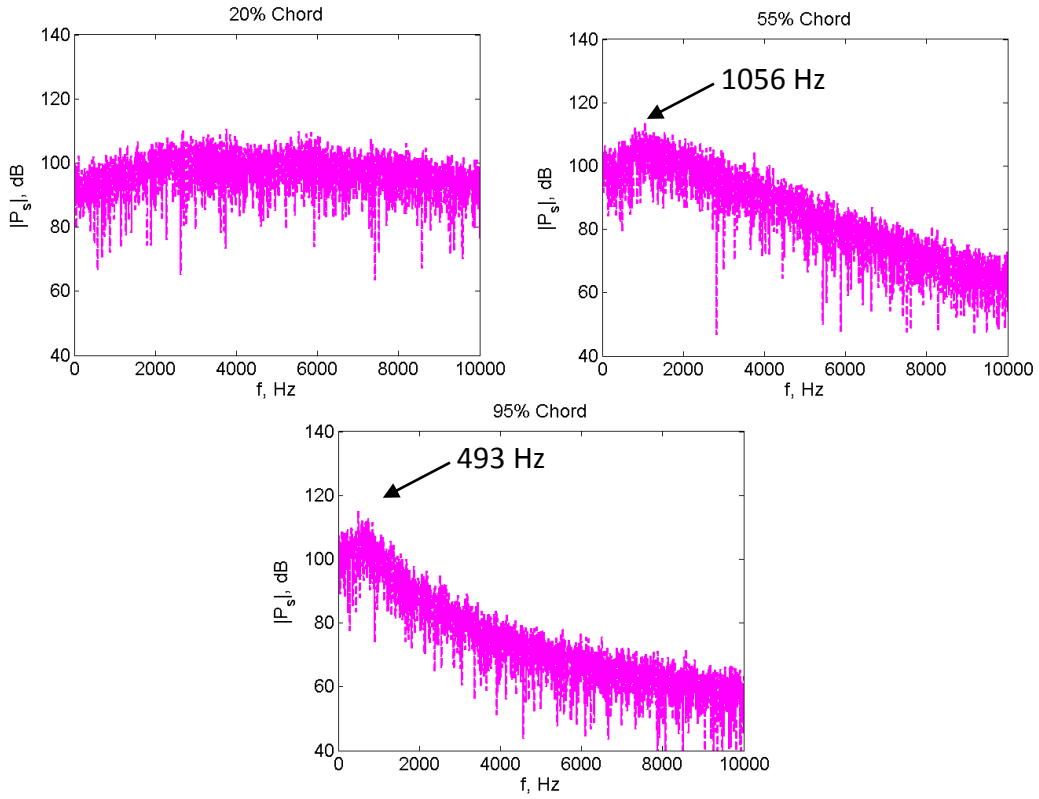

Figure 3.32. Suction surface wall pressure spectra at 10˚.

3.2.6. Proposed Interpretation of the Disappearance of Tones

1. With increasing incidence angles, the separation occurs on the suction surface towards the leading edge and its extent decreases with increasing the incidence angle (Figure 3.21).
2. The LST-calculated instability growth reaching the trailing edge is weaker for higher incidence angles. (Figure 3.26)
3. The LST does not predict a well-defined peak frequency for max amplification, and the growth rate tends to be only weakly dependent on the frequency (Figure 3.26).
4. Due to the unsteady flow near the trailing edge, the vortices to drift away from

the airfoil surface without interacting strongly with the trailing edge. Vortex shedding is not characterized by a clear shedding frequency (Figure 3.28), hence preventing scattering of acoustic waves of a consistent frequency at the trailing edge.

3.3. Effect of Reynolds Number at 2˚ Angle of Attack

A set of simulations were carried out for a range of Re at a fixed 2˚ angle of attack, as indicated by the red line in Figure 3.30, in order to investigate the role of instability growth on each surface as the Re changes. Results are shown for two cases: Re = 144,000, and Re = 288,000.

3.3.1. Tones

Tonal peaks were observed in the near-field spectrum for all simulations. Figure 3.31 and Figure 3.32 show the acoustic spectra at 2 chords above the trailing edge for the Re = 144,000 case and the Re = 288,000 case respectively. These spectra are calculated directly from the ILES code results. At Re = 144,000, there is a primary tone at 1049 Hz and an apparent harmonic tone at 2093 Hz. At Re = 288,000, there is a primary tone at 1768 Hz and harmonic tones present at 3536 Hz and 5300 Hz.

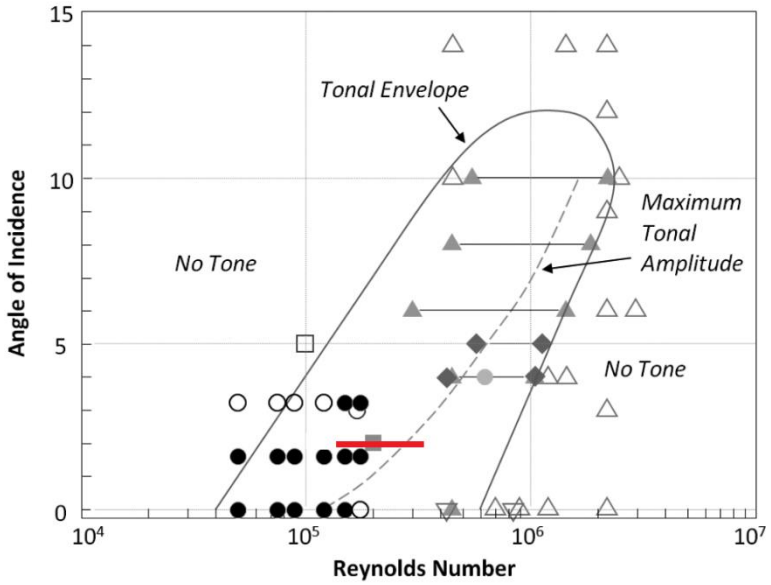

Filled markers represent that a tone was present, while unfilled markers represent that a tone was not present. Data sources: circles (Arcondloulis et al., 2009), triangles (Paterson et al., 1973), inverted triangles (Arbey and Bataille, 1983), squares, (Desquesnes et al., 2007), diamonds (Lowson et al., 1994), Tonal envelope and maximum amplitude line (Lowson et al., 1994).

Figure 3.33. Varying Re for fixed angle (Arcondoulis et al., 2010).

Table 3.4. Near-field tonal frequencies.

Reynolds	**Observed Tone (Hz)**
144,000	1049
180,000	1156
216,000	1542
252,000	1799
288,000	1768
324,000	1883
396,000	1959
468,000	2047

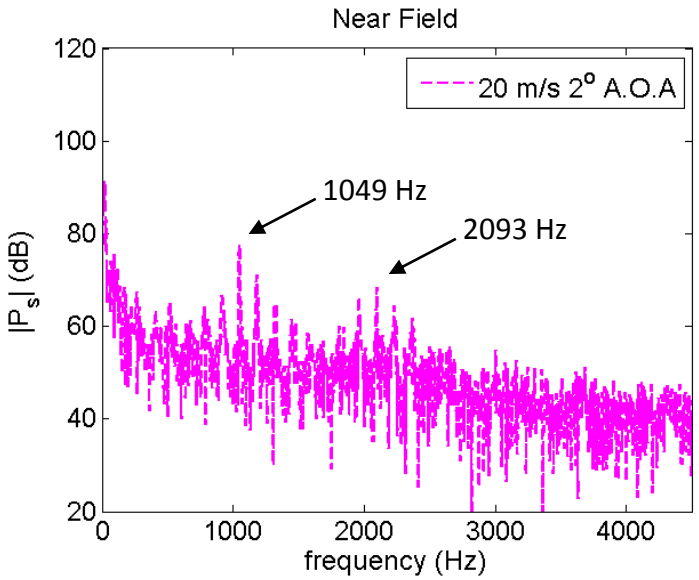

Figure 3.34. Near-field spectrum for Re = 144,000.

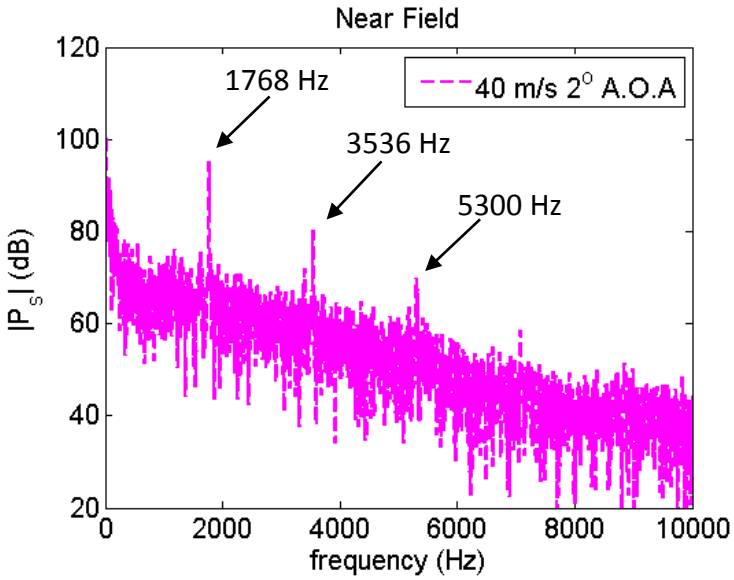

Figure 3.35. Near-field spectrum for Re = 288,000.

3.3.2. Separation Regions

As can be seen from Figure 3.34, there exist prominent separation regions on both surfaces of the airfoil at Re = 144,000. However, the separation regions on the suction

surface appears to diminish as the Re is increased. At Re = 144,000 the flow is separated from 52% to 80% (28%) chord on the suction surface. By Re = 288,000, this region has been reduced significantly to the space between 57% and 64% (17%) chord, as seen in Figure 3.35.

Conversely, the separated regions on the pressure surface remain approximately the same size for all velocities, though the C_f becomes increasingly negative near the TE as the velocity increases. The exact locations of the regions are given shown in Figure 3.36.

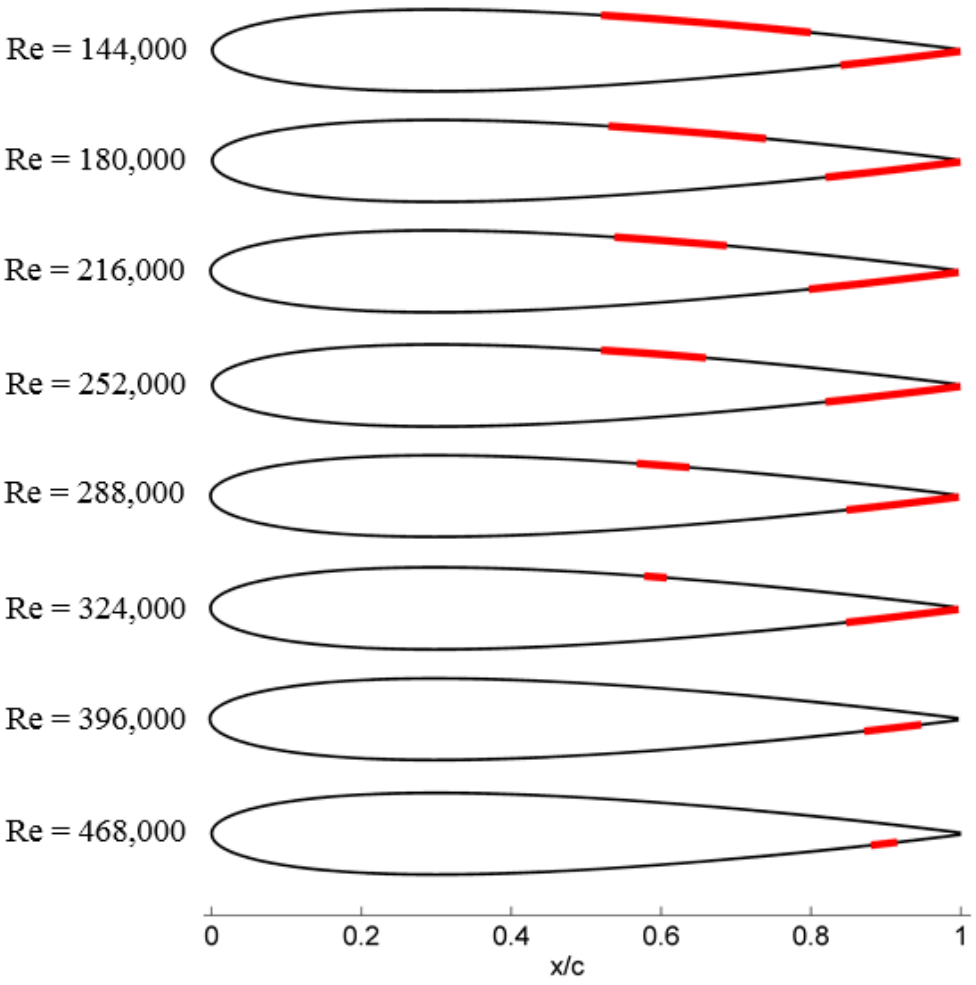

Figure 3.36. Separation Regions with Varied Re.

It is important to note that although the C_f no longer drops below 0 on the suction surface above Re = 324,000, there still exists a region where it is very close to 0 and a shear layer is still observed to be present, and hence the roll up of vortices is still observed on this surface at the highest Re observed in this study.

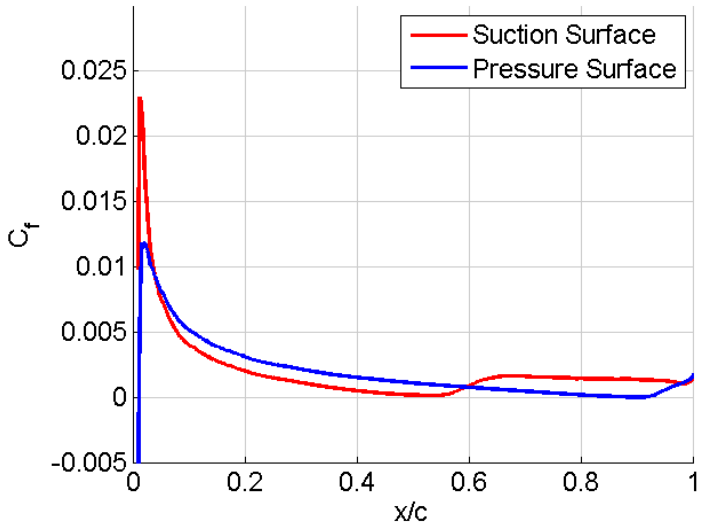

Figure 3.37. C_f at Re = 268,000.

Based on the observed trend of reducing size of the suction surface separation region with increased Re, it is expected that at some higher Re, this separation region will disappear entirely, leaving only the region on the pressure surface near the trailing edge, which has remained relatively unchanged within the range of observed Re.

3.3.3. The LST Results

At Re = 144,000, the predicted amplification on the suction surface is significantly higher than that on the pressure surface, but by Re = 288,000, the pressure surface has become similarly amplified. As seen in Figure 3.39, by Re = 468,000 the amplification on the pressure side has become more highly amplified for all frequencies below approximately 4000 Hz, which includes the observed tonal frequency.

In Figure 3.37 and Figure 3.38, the blue lines represent the maximum amplification on the suction surface and the red lines represent the maximum amplification on the pressure surface.

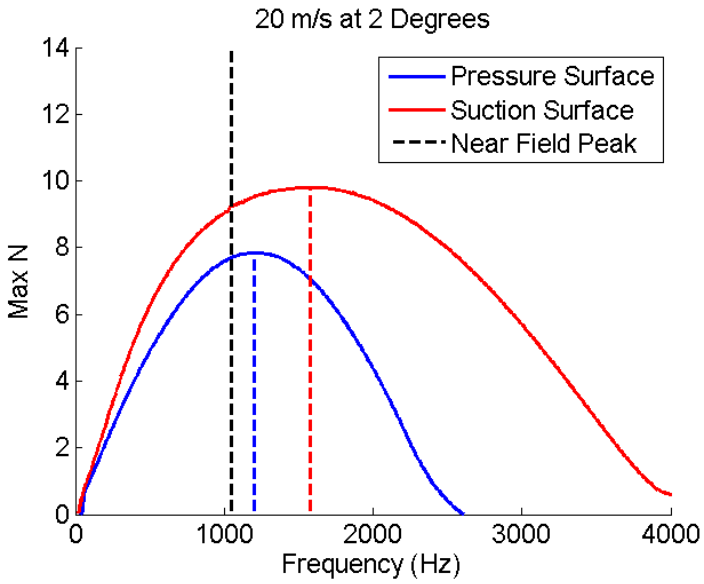

Figure 3.38. Peak N-factor for Re = 144,000.

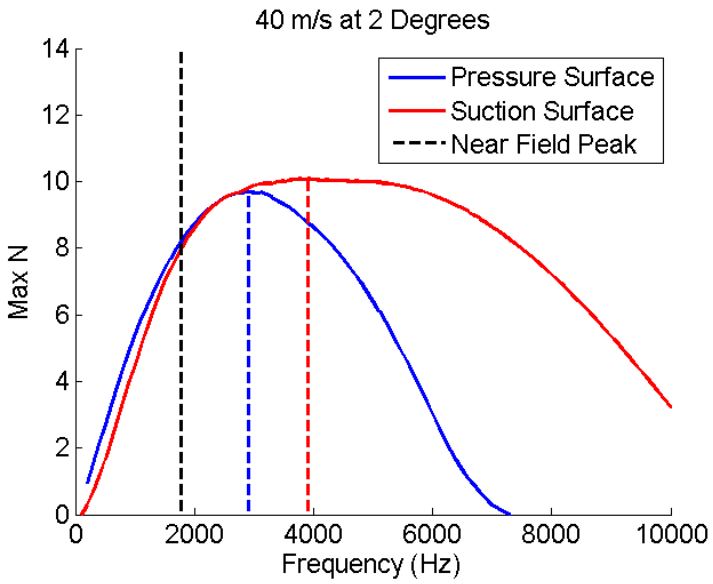

Figure 3.39. Peak N-factor for Re = 288,000.

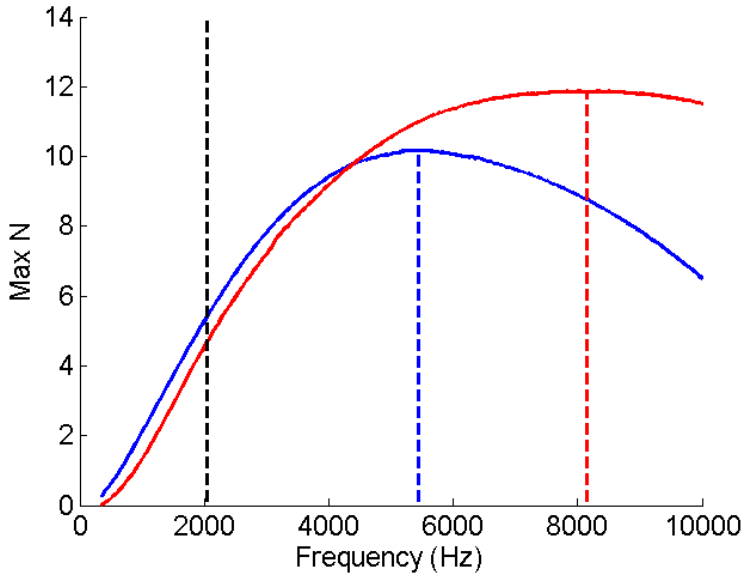

Figure 3.40. Peak N-factor for Re = 468,000.

Figure 3.41 through Figure 3.43 show more clearly how the amplification of the tonal frequency changes as Re is increased. At the lowest Re, the tonal frequency is significantly more amplified on the suction surface, but at the highest Re, the amplification on the pressure surface is approximately twice that of the suction surface.

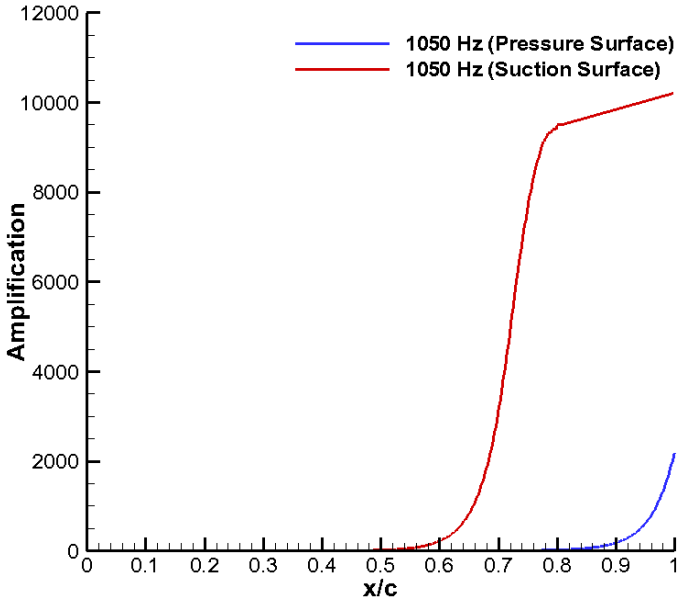

Figure 3.41. Chordwise amplification of tonal frequency for Re = 144,000.

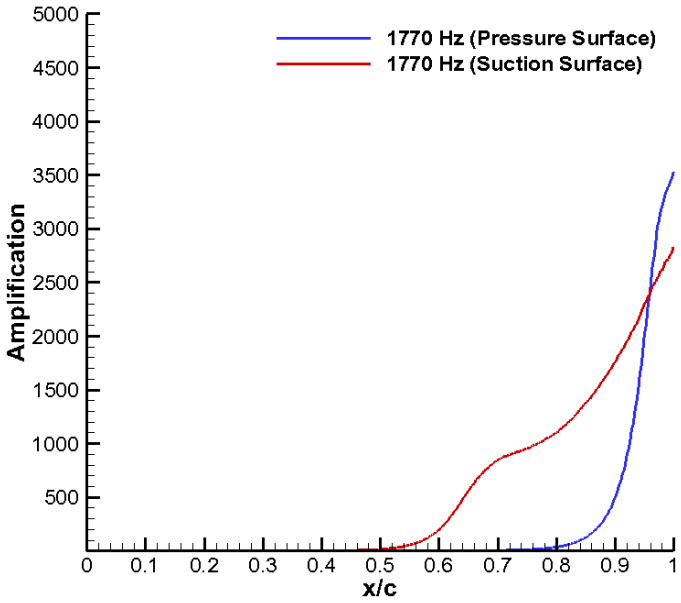

Figure 3.42. Chordwise amplification of tonal frequency for Re = 288,000.

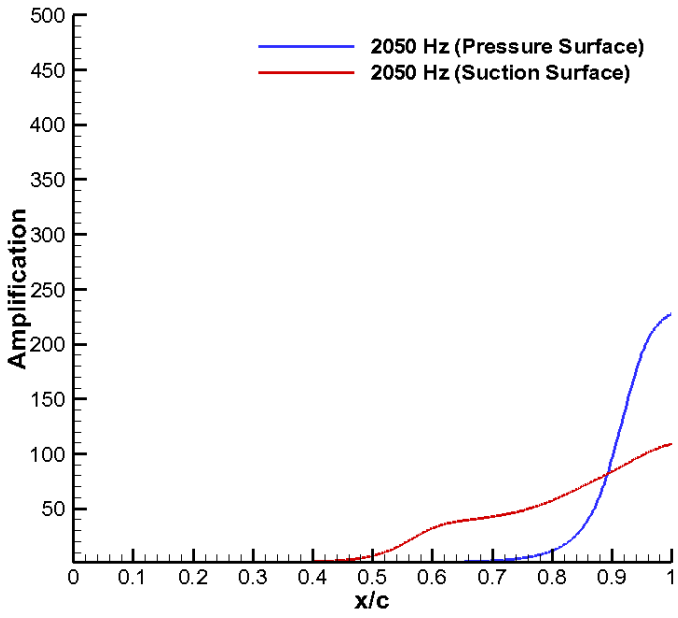

Figure 3.43. Chordwise amplification of tonal frequency for Re = 468,000.

3.3.4. Vorticity Contours

As can be seen from the vorticity contours in Figure 3.44 and 3.45, the change in predicted amplification is reflected in the vorticity contours. At Re = 144,000, the disturbances only roll up into vortices on the suction surface, while at Re = 288,000 vortex generation can be clearly seen on the pressure surface as well.

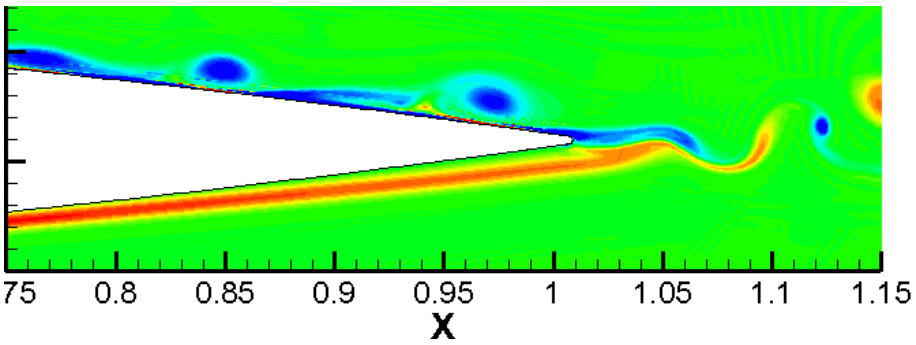

Figure 3.44. Vorticity contours for Re = 144,000.

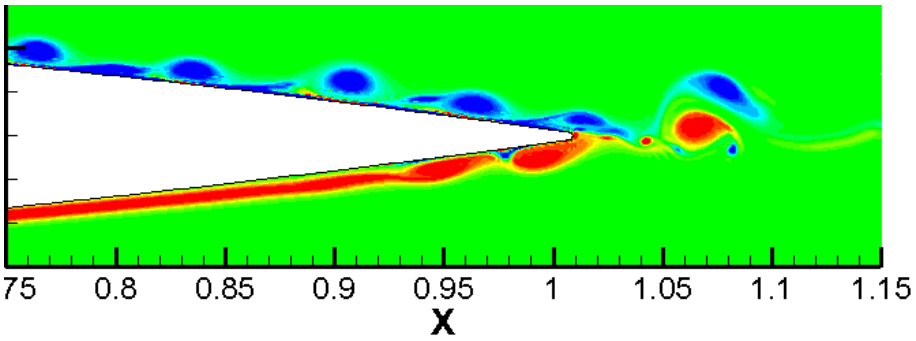

Figure 3.45. Vorticity contours for Re = 288,000.

3.3.5. Surface Pressure Spectra

The wall pressure spectra at 95% chord for each case are shown in Figure 3.46. The spectra at Re = 144,000 show that although the same peaks are present on both surfaces, the peaks on the suctions surface are approximately 10dB higher than on the pressure surface, indicating that the suction surface is the primary contributing source for the tonal noise. Conversely, at Re = 288,000, as seen in Figure 3.47, the peak pressure level on the pressure surface is slightly higher than that on the suction surface, indicating that at this higher Re, the pressure surface has a more significant role in the generation of tones.

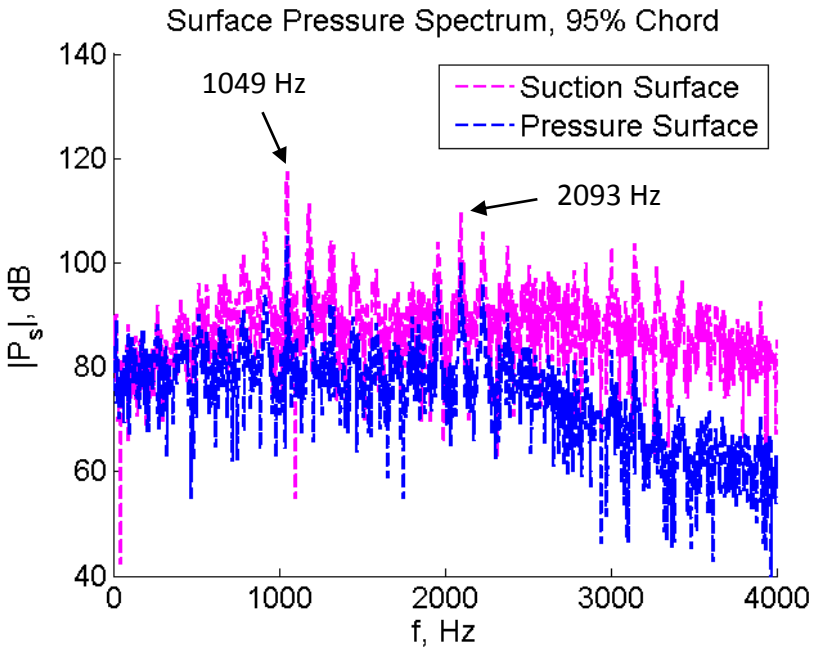

Figure 3.46. Wall pressure spectra for Re = 144,000

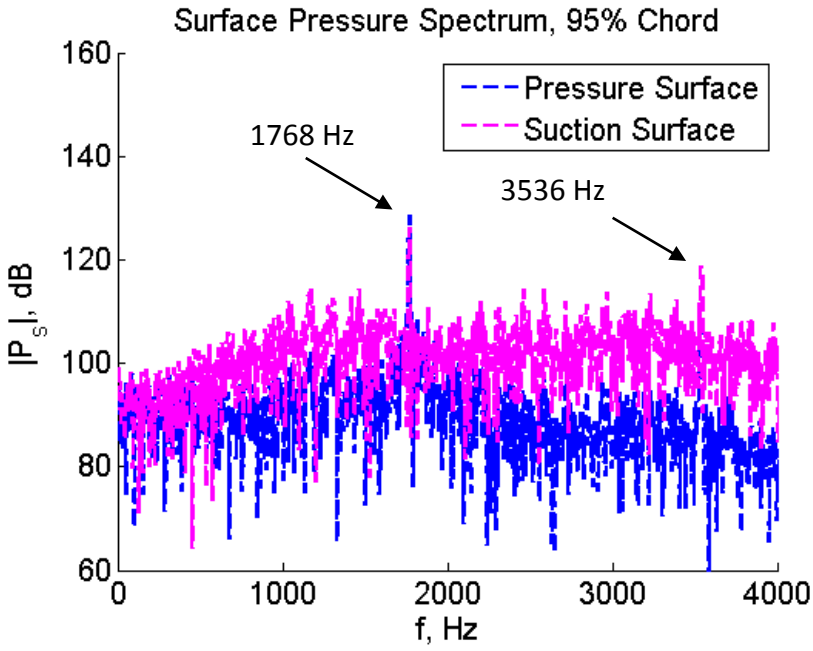

Figure 3.47. Wall pressure spectra for Re = 288,000

3.3.6. Proposed Interpretation of the Effect of Reynolds Number

For the incidence angle of 2˚, we have conducted the simulations for various Re. Our results can be summarized as follows.

1. For a low transitional at Re = 144,000, the separation on the suction side happens at the forward part of the airfoil and extends over a larger domain than that of the separation happening at the pressure side, which is restricted to the trailing edge region. As such, the suction surface tends to generate larger flow instability waves as compared to that generated by the lower surface. Thus, it is essentially the suction surface is the one contributing to the formation of the tonal noise. This can explain the experimental findings in Golubev et al. (2014), which show that at lower Re there was little difference in the spectrum between an untripped configuration and a configuration in which the pressure side was tripped to prevent the development of coherent instabilities on that surface.
2. As the Re increases, the extent of the separation region on the suction surface decreases and its generated flow instability waves at the trailing edge becomes weaker. With increasing Re a situation is reached where the flow instability generated by the suction and pressure side are more or less equal and both sides can contribute equally to the formation of the tones, and later the pressure side may be the only contributor at this Re range. This would explain the observations in Desquesnes et al. (2007) that the pressure side stability predictions were correlated well with the observed tone.
3. However, since the separation region diminishes with increasing Re, and the

amplified flow instability weakens, there is a limit for Re beyond which no tones are generated. This, in addition to the flow becoming turbulent earlier, can explain the experimental observational that the tones disappear altogether at high Re.

4. Conclusion

In order to better understand the mechanisms of tonal noise generation, a parametric study was carried out for a NACA0012 airfoil for varying Re and angles of attack. As shown by the far-field spectra in Figure 3.4, at Re = 180,000 tonal noise was observed between 0˚ and 6˚. It was also observed for all cases between Re = 144,000 and Re = 324,000. The observed flow features can be summarized as follows:

4.1. Confirmation of results from prior studies

1. Linear stability theory shows that there is a rapid increase in the amplification rate in the observed separation regions, as shown in Figure 3.7 through 3.10. It was observed that laminar separation regions exist on the pressure surface up to 4˚ and on the suction surface up to 12˚ at Re = 180,000. These regions:
    a. Correspond with the locations of high instability amplification, which explains the observed increase in RMS pressure.
    b. Provide a spectrum of various frequencies for disturbances to be amplified by linear instability growth or other possible mechanisms, since all frequencies experience rapid amplification within these regions.

2. For incidence angles above 0˚, Figure 3.12 through 3.14 show that the observed acoustic tones did not correspond well with the most amplified frequency predicted by LST. However,
    a. It is seen in Figure 3.18 that the tones correspond with the vortex shedding frequency for all tonal cases. Although the initial development of instabilities is linear, the roll-up of vortices could be significantly affected

by nonlinear processes.

b. This may be explained by the work of Jones and Sandberg (2011), in which it was found by the analytical application of Amiet's theory of trailing edge noise that the processes of receptivity and trailing-edge noise generation become increasingly efficient at lower frequencies. While LST can explain the initial growth of instabilities, it does not fully explain the mechanism of frequency selection. It is likely that the BL receptivity and TE scattering mechanisms have significant roles in the selection process.

4.2. New conclusions based on current work

3. The presence of tones was observed to persist as long as the vortex shedding remained well-ordered and attached at the trailing edge. With the cessation of tonal noise due to increased angle of attack, it is observed that:
    a. The separation region has moved very close to the leading edge, as seen in Figure 3.24.
    b. Vortex generation gives rise to small-scale turbulence near the leading edge, corresponding with the stability results in Figure 3.29 which predict that all frequencies are similarly amplified within the separation region.
    c. The primary cause of the cessation of tones is that flow near the trailing edge becomes highly unsteady at the higher angles, allowing the vortices to drift away from the airfoil surface without interacting with the trailing edge, thus preventing the scattering of acoustic waves at the TE.

4. At moderate incidence angles and low transitional Re (Re < 180,000), it appears

that the suction surface plays a key role in generating tones. As the angle increases, the suction surface may become the only source tone generation.

a. As demonstrated by the 6˚ case in Figure 3.3, tones can remain present despite the fact that no separation region exists on the pressure surface. At this angle, it was found that the acoustic tones corresponds not with the globally most amplified frequency, but with a frequency that remain unstable and highly amplified at the suction surface trailing edge, as shown in Figure 3.14.
b. In the 2˚ cases for Re = 144,000 and 180,000, where separation exists on both sides, the stability results in Figure 3.38 and 3.39 respectively predict higher amplification on the suction side than the pressure side.
c. This is supported by the wall pressure spectra in Figure 3.46 which shows that the amplitude of the peak pressure fluctuation on the suction surface is higher than on the pressure surface.

5. At higher transitional Re (Re > 288,000), we believe that instability growth on the pressure surface gains a larger role in tonal generation and becomes the primary source at sufficiently high Re.
    a. As the Re is increased at 2˚ angle of attack, the separation region on the suction surface diminishes, as seen in Figure 3.39, while the region on the pressure surface remains relatively unchanged.
    b. Likewise, Figure 3.40 indicates that stability analysis predicts an increasingly dominant role of instability growth on the pressure surface as

the Re is increased, particularly at low frequencies.

c. This conclusion is also supported by the peak frequencies observed in the wall pressure spectra in Figure 3.46 and 3.47, which show that at Re = 144,000 the suction surface pressure fluctuation has a higher amplitude, while at Re = 288,000 the peak pressure fluctuation on the pressure surface is of slightly higher amplitude.

5. Future Work

There are a few areas that would be of interested for continued study in order to clarify and expand upon some of the findings in this study. Jones and Sandberg (2011) used an analytical application of Amiet's theory of trailing edge noise in order to show that the TE noise generation process and receptivity process are more efficient at low frequencies. A similar analysis of the airfoil configurations studied herein would be appropriate to further investigate why the observed acoustic tones are lower than those predicted by Linear Stability theory.

The LASTRAC stability code is also capable of performing nonlinear stability analysis. It could be that the roll-up of vortices within the shear layer is significantly affected by nonlinear processes. Therefore, nonlinear stability analysis may also elucidate the mechanism of frequency selection.

Finally, it was also shown that as the Re increases, the separation region on the suction surface diminishes. However, the cases studied did not include a Re at which this separation region disappeared entirely. Analysis of the airfoil at higher Re could confirm this prediction and show that the tonal noise generation shifts entirely to the pressure surface at sufficiently high Re.

Further work is planned with an SD7003 airfoil to investigate the effects of geometry on the noise mechanisms.

The results presented here will also be compared with 3D simulations of certain cases in the future.

References

Amiet, R. (1976), "Noise due to turbulent flow past a trailing edge", Journal of Sound and Vibration, vol. 47, pp. 387-393.

Arbey, H., and Bataille, J. (1983). Noise generated by airfoil profiles placed in a uniform laminar flow. Journal of Fluid Mechanics, vol. 134, pp. 33-47.

Arcondoulis, E., Doolan, C., Zander, A., and Brooks, L. (2010, December). A review of trailing edge noise generated by airfoils at low to moderate Reynolds numbers. Acoustics Australia, vol. 38 (no. 3), pp. 135-139.

Arcondoulis, E., Doolan, C., Zander, A. (2009) "Airfoil Noise Measurement at Various Angles of Attack and Low Reynolds Numbers", Proceedings of Acoustics 2009, November 23-25, Adelaide, Australia.

Brooks, T. F., Pope, D. S., & Marcolini, M. A. (1989, July). Airfoil self-noise and prediction. NASA Reference Publication 1218.

Chang, Chau-Lyan (2004), Langley Stability and Transition and Analysis Code (LASTRAC) Version 1.2 User Manual, Langley Research Center, Hamption VA. NASA/TM-2004-213233

Clark, L.T. (1971), "The Radiation of Sound From Immersed Airfoils in a Laminar Flow." Trans ASMEA: Journal of Engineering Power, vol. 12, pp. 366-376.

Desquesnes, G., Terracol, M., and Sagaut, P. (2007). Numerical investigations of the tone noise mechanism over laminar airfoils. Journal of Fluid Mechanics, vol. 591, 155{182. doi: 10.1017/S0022112007007896.

Doolan, C. (2008). A review of airfoil trailing edge noise and its prediction. Acoustics Australia, vol. 36 (no. 1), pp. 7-13.

Ffowcs Williams, J. E. and Hawkings, D. L. (1969), Sound Generation by Turbulence and Surfaces in Arbitrary Motion, Proceedings of the Royal Society of London, Series A: Mathematical and Physical Sciences, 264(1151), pp. 321–342.

Gaitonde, D. V., and Visbal, M. R. (1998), "High-Order Schemes for Navier-Stokes Equations: Algorithm and Implementation into FDL3DI," Air Force Research Laboratory Tech. Rep. TR-1998-3060, Wright-Patterson Air Force Base, Ohio.

Golubev, V.V., Nguyen, L., Mankbadi, R.R., Roger, M., and Visbal, M.R., (2014) "On Flow-Acoustic Resonant Interactions in Transitional Airfoils," International Journal of Aeroacoustics, Vol. 13, pp. 1-38.

Jones, L. E., Sandberg, R. D. (2010), "Stability and Receptivity characteristics of a

laminar separation bubble on an aerofoil." Journal of F, vol. 648, pp. 257 – 296.

Jones, L. E., Sandberg, R. D. (2011), "Numerical Analysis of Tonal Airfoil Self-Noise and Acoustic Feedback-Loops." Journal of Sound and Vibration, vol. 330, 6137 – 6152.

Lele, S. K. (1992), Compact Finite Difference Schemes with Spectral-Like Resolution, Journal of Computational Physics, 103(1), pp. 16–42.

Lowson, M. V., Fiddes, S. P., and Nash, E. C. (1994), "Laminar Boundary Layer Aeroacoustic Instabilities", AIAA Paper 94-0358, 32nd Aerospace Sciences Meeting and Edhibition, Reno.

Lyrintzis, A.S. (2003), "Surface integral methods in computational aeroacoustics – From the (CFD) near-field to the (Acoustic) far-field. International Journal of Aeroacoustics, Vol. 3, no. 4, pp. 297-346.

Mankbadi, R. R., Wu, X., and Lee, S. S. (1993) "A Critical-Layer Analysis of the Resonant Triad in Boundary-Layer Transition: Nonlinear Interactions," Journal of Fluid Mechanics, Vol. 256, pp. 85-106.

Nash, E. C., Lowson, M. V., & McAlpine, A. (1999). Boundary-layer instability noise on aerofoils. Journal of Fluid Mechanics, vol. 382, pp. 27-61.

Patterson, R., Vogt, P., Fink, M., & Munch, C. (1973). Vortex noise of isolated airfoils. Journal of Aircraft, vol. 36, pp. 296-302.

Rizzetta, D. P., Visbal, M. R., and Stanek, M. J. (1999), "Numerical Investigation of Synthetic-Jet Flow Fields," AIAA J., Vol. 37, pp. 919-927.

Tam, C. K. (1974). Discrete tones of isolated airfoils. Journal of the Acoustical Society of America, vol. 55 (no. 6, June), pp. 1173-1177.

Visbal, M. R., and Gaitonde, D. V. (2002), "On the use of High-Order Finite-Difference Schemes on Curvilinear and Deforming Meshes," Journal of Computational Physics, Vol. 181, pp. 155–185.